



CHALMERS

Chalmers Publication Library

VELOCITY-RESOLVED [C II] EMISSION AND [C II]/FIR MAPPING ALONG ORION WITH HERSCHEL

This document has been downloaded from Chalmers Publication Library (CPL). It is the author's version of a work that was accepted for publication in:

Astrophysical Journal (ISSN: 0004-637X)

Citation for the published paper:

Goicoechea, J. ; Teyssier, D. ; Etxaluze, M. et al. (2015) "VELOCITY-RESOLVED [C II] EMISSION AND [C II]/FIR MAPPING ALONG ORION WITH HERSCHEL".
Astrophysical Journal, vol. 812 pp. 75.

Downloaded from: <http://publications.lib.chalmers.se/publication/225568>

Notice: Changes introduced as a result of publishing processes such as copy-editing and formatting may not be reflected in this document. For a definitive version of this work, please refer to the published source. Please note that access to the published version might require a subscription.

Chalmers Publication Library (CPL) offers the possibility of retrieving research publications produced at Chalmers University of Technology. It covers all types of publications: articles, dissertations, licentiate theses, masters theses, conference papers, reports etc. Since 2006 it is the official tool for Chalmers official publication statistics. To ensure that Chalmers research results are disseminated as widely as possible, an Open Access Policy has been adopted. The CPL service is administrated and maintained by Chalmers Library.

(article starts on next page)

VELOCITY-RESOLVED [C II] EMISSION AND [C II]/FIR MAPPING ALONG ORION WITH *HERSCHEL**†

JAVIER R. GOICOECHEA¹, D. TEYSSIER², M. ETXALUZE^{1,3}, P. F. GOLDSMITH⁴, V. OSSENKOPF⁵, M. GERIN^{6,7}, E. A. BERGIN⁸, J. H. BLACK⁹, J. CERNICHARO¹, S. CUADRADO¹, P. ENCRENAZ⁶, E. FALGARONE^{6,7}, A. FUENTE¹⁰, A. HACAR¹¹, D. C. LIS⁶, N. MARCELINO¹², G. J. MELNICK¹³, H. S. P. MÜLLER⁵, C. PERSSON⁹, J. PETY¹⁴, M. RÖLLIG⁵, P. SCHILKE⁵, R. SIMON⁵, R. L. SNELL¹⁵, AND J. STUTZKI⁵

¹ Instituto de Ciencia de Materiales de Madrid (CSIC), Calle Sor Juana Ines de la Cruz 3, E-28049 Cantoblanco, Madrid, Spain; jr.goicoechea@icmm.csic.es

² Herschel Science Centre, ESA/ESAC, P.O. Box 78, Villanueva de la Cañada, E-28691 Madrid, Spain

³ RAL Space, Rutherford Appleton Laboratory, Didcot OX11 0QX, UK

⁴ Jet Propulsion Laboratory, California Institute of Technology, 4800 Oak Grove Drive, Pasadena, CA 91109-8099, USA

⁵ I. Physikalisches Institut der Universität zu Köln, Zùlpicher Str. 77, D-50937 Köln, Germany

⁶ LERMA, Observatoire de Paris, PSL Research University, CNRS, Sorbonne Universités, UPMC Univ. Paris 06, F-75014, Paris, France

⁷ École Normale Supérieure, 24 rue Lhomond, F-75005, Paris, France

⁸ Department of Astronomy, University of Michigan, 500 Church Street, Ann Arbor, MI 48109, USA

⁹ Department of Earth and Space Sciences, Chalmers University of Technology, Onsala Space Observatory, SE-43992 Onsala, Sweden

¹⁰ Observatorio Astronómico Nacional (OAN IGN), Apdo. 112, E-28803, Alcalá de Henares, Spain

¹¹ Institute for Astrophysics, University of Vienna, Türkenschanzstrasse 17, A-1180, Vienna, Austria

¹² INAF, Istituto di Radioastronomia, via P. Gobetti 101, I-40129, Bologna, Italy

¹³ Harvard-Smithsonian Center for Astrophysics, 60 Garden Street, MS 66, Cambridge, MA 02138, USA

¹⁴ Institut de Radioastronomie Millimétrique, 300 rue de la Piscine, F-38406 Saint-Martin d'Héères, France

¹⁵ Department of Astronomy, University of Massachusetts, LGRT-B 619E, 710 North Pleasant Street, Amherst, MA 01003, USA

Received 2015 May 27; accepted 2015 August 12; published 2015 October 9

ABSTRACT

We present the first $\sim 7!5 \times 11!5$ velocity-resolved ($\sim 0.2 \text{ km s}^{-1}$) map of the [C II] 158 μm line toward the Orion molecular cloud 1 (OMC 1) taken with the *Herschel*/HIFI instrument. In combination with far-IR (FIR) photometric images and velocity-resolved maps of the H41 α hydrogen recombination and CO $J = 2-1$ lines, this data set provides an unprecedented view of the intricate small-scale kinematics of the ionized/photodissociation region (PDR)/molecular gas interfaces and of the radiative feedback from massive stars. The main contribution to the [C II] luminosity ($\sim 85\%$) is from the extended, FUV-illuminated face of the cloud ($G_0 > 500$, $n_{\text{H}} > 5 \times 10^3 \text{ cm}^{-3}$) and from dense PDRs ($G_0 \gtrsim 10^4$, $n_{\text{H}} \gtrsim 10^5 \text{ cm}^{-3}$) at the interface between OMC 1 and the H II region surrounding the Trapezium cluster. Around $\sim 15\%$ of the [C II] emission arises from a different gas component without a CO counterpart. The [C II] excitation, PDR gas turbulence, line opacity (from [¹³C II]), and role of the geometry of the illuminating stars with respect to the cloud are investigated. We construct maps of the $L[\text{C II}]/L_{\text{FIR}}$ and $L_{\text{FIR}}/M_{\text{Gas}}$ ratios and show that $L[\text{C II}]/L_{\text{FIR}}$ decreases from the extended cloud component ($\sim 10^{-2}-10^{-3}$) to the more opaque star-forming cores ($\sim 10^{-3}-10^{-4}$). The lowest values are reminiscent of the “[C II] deficit” seen in local ultraluminous IR galaxies hosting vigorous star formation. Spatial correlation analysis shows that the decreasing $L[\text{C II}]/L_{\text{FIR}}$ ratio correlates better with the column density of dust through the molecular cloud than with $L_{\text{FIR}}/M_{\text{Gas}}$. We conclude that the [C II]-emitting column relative to the total dust column along each line of sight is responsible for the observed $L[\text{C II}]/L_{\text{FIR}}$ variations through the cloud.

Key words: galaxies: ISM – H II regions – infrared: galaxies – ISM: clouds

1. INTRODUCTION

The $^2P_{3/2}-^2P_{1/2}$ fine-structure line ($\Delta E/k \simeq 91 \text{ K}$) of ionized carbon, [C II] 158 μm , is one of the most important cooling lines of the cold neutral medium (Dalgarno & McCray 1972) and among the brightest lines in photodissociation regions (PDRs; e.g., Hollenbach & Tielens 1999). Early observations showed that the line is very luminous (Russell et al. 1980), carrying from $\sim 0.1\%$ to 1% of the total far-IR (FIR) luminosity of galaxies (Crawford et al. 1985). The neutral carbon atom has an ionization potential of 11.3 eV, so that the ion C^+ traces the H^+/H_2 transition, the critical conversion from atomic to molecular ISM. As a consequence, [C II] emission/absorption from different ISM phases is expected. Recent velocity-resolved line surveys show that the

average contribution to the [C II] emission in the Milky Way is the H_2 gas illuminated by far-UV (FUV; $E \simeq 6-13.6 \text{ eV}$) photons (55%–75%), the cold atomic gas (20%–25%), and the H II ionized gas (5%–20%) (Pineda et al. 2013, 2014).

Star-forming complexes hosting massive OB stars are irradiated by strong FUV fields, and most of their [C II] emission is likely to arise from dense PDRs at the interface between H II regions and their parental molecular cloud (e.g., Stacey et al. 1993). Therefore, the [C II] 158 μm line traces the FUV radiation field from massive stars and, indirectly, the star formation rate (SFR) (e.g., Stacey et al. 2010; Pineda et al. 2014; Herrera-Camus et al. 2015). As in the Milky Way, the [C II] emission in nearby galaxies is widespread and ultimately related to the star formation activity (Malhotra et al. 2001; Rodríguez-Fernández et al. 2006; Kapala et al. 2015). In addition, an undetermined fraction of the [C II] arises from the diffuse neutral gas (Madden et al. 1993) and from the H II ionized gas, the latter varying from $\sim 5\%$ to 50% , depending on the ionizing radiation strength and electron density (e.g., Abel 2006a).

* *Herschel* is an ESA space observatory with science instruments provided by European-led Principal Investigator consortia and with important participation from NASA.

† Uses observations obtained with the IRAM 30 m telescope. IRAM is supported by INSU/CNRS (France), MPG (Germany), and IGN (Spain).

In normal and starburst galaxies, the [C II]-to-FIR luminosity¹⁶ ratio ($L[\text{C II}]/L_{\text{FIR}}$) is in the 10^{-2} to 10^{-3} range. Low-metallicity dwarf galaxies show the highest ratios ($\gtrsim 10^{-2}$; e.g., Madden et al. 1997), whereas observations with the *Infrared Space Observatory* showed that local ultraluminous galaxies (ULIRGs, $L_{\text{FIR}} > 10^{12} L_{\odot}$) display a deficiency, $L[\text{C II}]/L_{\text{FIR}} \simeq 10^{-4}$, that is not straightforward to interpret (Malhotra et al. 1997; Luhman et al. 1998). This fractional luminosity deficiency has been confirmed with new observations of ULIRGs, hosting intense star formation and often associated with galaxy mergers (e.g., Graciá-Carpio et al. 2011; González-Alfonso et al. 2015). This deficit, however, does not necessarily hold in the early universe at high z (e.g., Stacey et al. 2010; Brisbin et al. 2015).

Interestingly, while it is difficult from the ground to detect the [C II] emission in the local universe (balloon, airborne, or space telescopes are needed to overcome the low atmospheric transmission at $158 \mu\text{m}$), the line does become accessible to ground-based submillimeter observatories such as ALMA at redshifts $z > 1$. Indeed, the [C II] line has been detected toward young $z > 5$ galaxies (Riechers et al. 2014; Capak et al. 2015).

Most of the [C II] emission arising from PDR gas in the Milky Way is associated with modest average FUV radiation fields, between $G_0 \simeq 1$ –20 (Pineda et al. 2013) and $G_0 \simeq 100$ (Cubick et al. 2008), with G_0 the mean interstellar FUV field in Habing units ($G_0 = 1$ is equal to $1.6 \times 10^{-3} \text{ erg cm}^{-2} \text{ s}^{-1}$; Habing 1968). These radiation fields are likely not representative of the efficient massive star-forming modes expected in ULIRGs showing $L[\text{C II}]/L_{\text{FIR}}$ deficits. Galactic high-mass star-forming regions, however, offer a more interesting template in which to investigate the [C II] emission in the more extreme irradiation conditions prevailing in these active galaxies. The Orion molecular cloud 1 (OMC 1), in the Orion A complex, lies behind the Orion Nebula cluster (e.g., O’Dell 2001) and is the nearest (~ 414 pc) and probably most studied high-mass star-forming region of the Milky Way (e.g., Genzel & Stutzki 1989).

OMC 1 is directly exposed to the UV radiation emitted by young massive stars in the Trapezium cluster, located ~ 0.3 pc in front of the molecular cloud (e.g., Bally 2008). A region of several parsecs in size is exposed to FUV fluxes much higher than the average G_0 in the Milky Way (e.g., Stacey et al. 1993; Luhman et al. 1994; Rodríguez-Franco et al. 1998). The Trapezium stars have created a blister H II region that on the far side is bounded by the molecular cloud. The most famous H II/OMC 1 interface is the Orion Bar PDR (the Bright Bar seen in the visible-light images), a protrusion of OMC 1 in which the neutral cloud acquires a nearly edge-on geometry and thus the optically thin PDR emission is limb-brightened (Hogerheijde et al. 1995; Cuadrado et al. 2015, and references therein). On the near side, toward the observer, several components of neutral atomic gas revealed by H I absorption cover the nebula, the Orion’s Veil (e.g., van der Werf et al. 2013). Intermediate- and high-mass star formation is currently taking place in two locations: the Becklin–Neugebauer/Kleinmann–Low (BN/KL) region within OMC 1 (Blake et al. 1987; Tercero et al. 2010), and Orion south (S), an isolated molecular core located within

the ionized gas cavity in front of OMC 1 (e.g., O’Dell et al. 2009). Therefore, Orion is a unique region to study the spatial distribution of [C II] and related quantities ($L[\text{C II}]/L_{\text{FIR}}$, $L[\text{C II}]/L_{\text{CO}}$, $L_{\text{FIR}}/M_{\text{Gas}}$, etc.) in well-characterized environments (dense PDRs, shocks, H II regions, and lower-density quiescent gas).

The [C II] $158 \mu\text{m}$ line has been previously mapped toward OMC 1 at low angular ($\sim 55''$) and spectral ($\sim 67 \text{ km s}^{-1}$) resolution with the Kuiper Airborne Observatory (KAO; Stacey et al. 1993; Herrmann et al. 1997) and also with balloon-borne FIR telescopes (e.g., Mookerjee et al. 2003). Pointed observations toward the Trapezium cluster region were also carried out by Boreiko & Betz (1996) with a heterodyne receiver on board KAO. These observations employed a velocity resolution of 0.5 km s^{-1} and allowed the detection of two of the three [¹³C II] hyperfine line components. The HIFI instrument (de Graauw et al. 2010) on board *Herschel* (Pilbratt et al. 2010) allowed us to spectrally resolve ($\sim 0.2 \text{ km s}^{-1}$ resolution) and to map the [C II] $158 \mu\text{m}$ line with unprecedented sensitivity and angular resolution ($\sim 11''$). Velocity-resolved spectroscopy offers the best way to characterize the origin of all possible [C II] emission components and their kinematics. In addition, it allows one to map [¹³C II] and estimate the [C II] line opacity, a critical parameter to determine C⁺ column densities (Stacey et al. 1991b; Boreiko & Betz 1996; Goldsmith et al. 2012; Ossenkopf et al. 2013).

In this work, we present initial results from a *Herschel* Open-Time program (OT1_jgoicoec_4) devoted to the spatial and velocity structure of the ionized and the warm molecular gas in OMC 1. In particular, we present a large-scale velocity-resolved map of the [C II] $158 \mu\text{m}$ line, complemented by a map of the H41 α recombination line, and existing CO $J = 2$ –1 and FIR photometric observations. The paper is organized as follows. In Section 2 we present the data set. The [C II] spatial distribution and gas kinematics are studied in Section 3. In Section 4 we analyze the [C II] $158 \mu\text{m}$ non-LTE excitation and derive C⁺ column densities. A spatial correlation analysis of different quantities often used in the extragalactic discussion is also carried out. Finally, our results are discussed in the context of the [C II], CO, and FIR diagnostic power and their link with the extragalactic emission.

2. OBSERVATIONS AND DATA REDUCTION

2.1. [C II], H41 α , and CO 2–1 Heterodyne Observations

The [C II] line at 1900.537 GHz (Cooksy et al. 1986) was mapped over a total area of $\sim 7'.5 \times 11'.5$ ($\sim 0.9 \text{ pc} \times 1.4 \text{ pc}$) in 2012 August, using the HIFI instrument on board *Herschel*. A pair of Hot Electron Bolometer mixers was employed to observe the [C II] line in HIFI band 7b in two orthogonal polarizations. We used the Wide Band Acousto-Optical Spectrometer, providing a spectral resolution of 1.1 MHz and a bandwidth of 2.4 GHz ($\simeq 0.2 \text{ km s}^{-1}$ and $\simeq 380 \text{ km s}^{-1}$ at 1900.5 GHz, respectively).

Three $\sim 7'.5 \times 4'$ On-The-Fly (OTF) submaps of 3 hr each were needed to cover the region with a $10''$ sampling (ObsIDs: 1342250415, 1342250414, and 1342250412). The half-power beam width (HPBW) of HIFI at these frequencies is $\sim 11''$, i.e., the map is not fully sampled. Because of the large-scale [C II] emission (Stacey et al. 1993) and risk of contaminating emission in the reference position, the OTF maps were performed using the Load-Chop referencing scheme (Roelfsema

¹⁶ In this work we refer to the *luminosity* (L) computed in power units (erg s^{-1} or L_{\odot}). The conversion from velocity-integrated line intensities $\int \Delta T_b dv = W$ (K km s^{-1}), with ΔT_b the continuum-subtracted brightness temperature (see Section 2), to line surface brightness (I) is $I = 2k W \nu^3 / c^3$. For the [C II] $158 \mu\text{m}$ and CO $J = 2$ –1 lines, respectively, the conversion is I ($\text{erg s}^{-1} \text{ cm}^{-2} \text{ sr}^{-1}$) = $7.0 \times 10^{-6} W$ (K km s^{-1}) and $1.3 \times 10^{-8} W$ (K km s^{-1}).

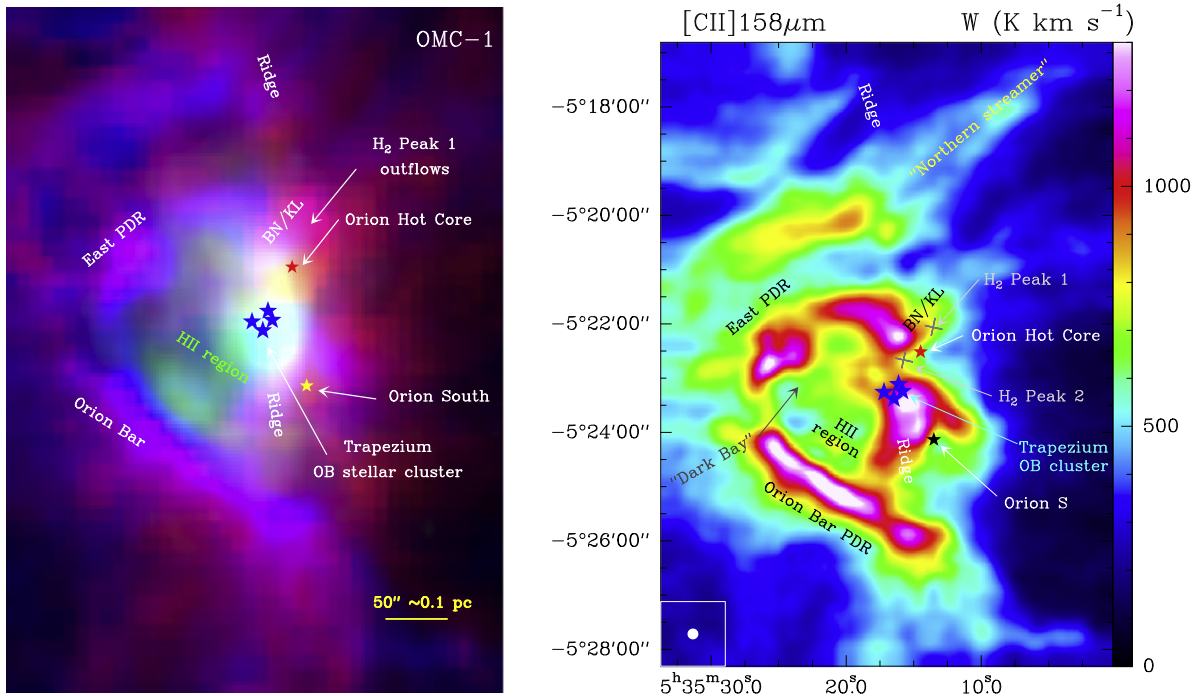


Figure 1. Left: Composite image with the H41 α (green), [C II] 158 μ m (blue), and CO 2–1 (red) integrated line intensities. The positions of the main sources in OMC 1 are shown. Right: *Herschel*/HIFI map of the total [C II] 158 μ m integrated line intensity¹⁶ (in K km s⁻¹) from $v_{\text{LSR}} = -30$ to $+30$ km s⁻¹.

et al. 2012). In this mode, an internal chopper alternates between the sky and an internal cold load as the telescope slews over a scan leg. Although a nearby reference position (at a radial offset of $\sim 9'$ from the map center) was also observed, we reprocessed the data without subtracting this reference emission from the on-source data, therefore being insensitive to line contamination from self-chopping. The resulting data are mostly affected by so-called Electrical Standing Waves, which were removed in HIPE¹⁷ using the *doHebCorrection* task (Kester et al. 2014). The residual optical standing waves resulting from resonances against the internal hot load (~ 100 MHz period) and the diplexer optics (~ 625 MHz) were treated using the *FitHifi-Fringe* task in HIPE. The three sub-maps were then compared pair by pair in a region of $\sim 7.5 \times 0.6$ where they overlap on the sky. Antenna temperatures (T_A^*) were extracted for each overlapping pixel and [C II] velocity channel. Scatter plots were formed to derive the inter calibration factor between the respective coverage in each channel. We derived linear slopes deviating from unity by $\sim 5\%$ between pairs of sub-maps. Since we cannot know a priori which map corresponds to the true intensity, we readjusted the fluxes by $\pm 2.5\%$ depending on the sub-map, i.e., recalibrated with respect to the mean intensities in the overlapping regions.

Through this work we use the main-beam temperature scale (T_{mb} in K) as opposed to T_A^* . Given the latest HIFI efficiencies, both scales¹⁸ are related by $T_{\text{mb}} \simeq 1.64 T_A^*$. For semi-extended (not infinite but larger than the main beam width of *Herschel*/HIFI) emission sources of uniform brightness temperature (T_b), the main-beam temperature is the most appropriate intensity scale ($T_{\text{mb}} \simeq T_b$). The achieved rms noise was typically ~ 1.5 K

(1σ) per 0.2 km s⁻¹ resolution channel and position. This rms is only a factor of ~ 2.5 worse than that achieved by Boreiko & Betz (1996) in their deep pointed observations after an integration of ~ 3 hr. Figure 1 (right) shows the baseline-subtracted [C II] integrated line intensity map.

The H41 α millimeter recombination line at 92.034 GHz was mapped with the IRAM 30 m telescope at Pico Veleta (Spain) using the E090 receiver and the 200 kHz FFTS backend in 2013 November. The HPBW at this frequency is $\sim 27''$, and the typical rms noise in the map is low, ~ 0.05 K per 0.65 km s⁻¹ resolution channel. In this work we also make use of part of the high-sensitivity CO 2–1 large-scale map ($1^\circ \times 0^\circ 8$) at 230.538 GHz obtained by Berné et al. (2014) with the multibeam receiver HERA, also at the IRAM 30 m telescope. The spectral and angular resolutions are 320 kHz and $\sim 11''$, respectively. The achieved rms noise is $\simeq 0.2$ K per 0.4 km s⁻¹ channel (see Berné et al. 2014). Both H41 α and CO 2–1 OTF maps are fully sampled.

Herschel/HIFI and IRAM 30 m data were processed with the GILDAS/CLASS software. Figures 1, 6, and 7 show the [C II] 158 μ m, H41 α , and CO 2–1 emission at their native angular resolutions but resampled to a common velocity grid of 0.65 km s⁻¹. Offsets of selected positions are given with respect to the center of the [C II] map: α_{2000} : $5^{\text{h}}35^{\text{m}}17^{\text{s}}.0$, δ_{2000} : $-5^\circ 22' 33''.7$. Table 1 summarizes the main spectroscopic parameters of the lines discussed in this work. To match the FIR photometric observations and carry out a combined analysis, the line maps were also gridded and convolved to a uniform angular resolution of $25''$ (~ 0.05 pc).

2.2. Photometric Observations and SED Fits

In order to determine the FIR luminosity¹⁹ and the dust continuum opacity toward each position of the [C II] map, we

¹⁷ HIPE is a joint development by the Herschel Science Ground Segment Consortium, consisting of ESA, the NASA Herschel Science Center, and the HIFI, PACS, and SPIRE consortia.

¹⁸ See http://herschel.esac.esa.int/twiki/pub/Public/HifiCalibrationWeb/HifiBeamReleaseNote_Sep2014.pdf.

¹⁹ L_{FIR} from 40 to 500 μ m (Sanders & Mirabel 1996) and using $D = 414$ pc.

Table 1
Spectroscopic Parameters of the Lines Discussed in This Work

Species	Transition	Frequency (GHz)	E_u/k (K)	A_{ij} (s^{-1})
$^{12}\text{C}^+$	$^2P_{3/2}-^2P_{1/2}$	1900.5369 ^a	91.21	2.32(-6)
$^{13}\text{C}^+$	$^2P_{3/2}-^2P_{1/2}$			
	$F = 1-0$	1900.9500 ^{a,b}	91.23	1.55(-6)
	$F = 2-1$	1900.4661 ^{a,b}	91.25	2.32(-6)
	$F = 1-1$	1900.1360 ^{a,b}	91.23	7.73(-7)
CO	$J = 2-1$	230.5379	16.60	6.92(-7)
H41 α	$n = 42-41$	92.0344 ^c	89.50	4.85(+1)

Notes.

^a From Cooksy et al. (1986).

^b See Ossenkopf et al. (2013) for corrected relative line strengths.

^c From Lilley & Palmer (1968).

also make use of fully sampled calibrated images of OMC 1 taken with the *Herschel*/SPIRE and PACS²⁰ cameras (Griffin et al. 2010; Poglitsch et al. 2010) at 70, 160, 250, and 350 μm photometric bands (from programs GT2_pandre and OT1_nbillot), and with JCMT/SCUBA2 at 850 μm (project JCMTCAL; Holland et al. 2013).

We convolved all the photometric images to a 25'' resolution (that of the 350 μm image) and fitted the resulting spectral energy distribution (SED) per 12''.5 pixel with a modified blackbody at an *effective* dust temperature (T_d):

$$F_\lambda = B_\lambda(T_d) \cdot (1 - e^{-\tau_{d,\lambda}}) \cdot \Omega, \quad (1)$$

where Ω is the solid angle subtended by each pixel. Fit examples are shown in the Appendix (see Figure 17). The dust continuum opacity is parameterized as $\tau_{d,\lambda} = \tau_{d,160}(160/\lambda)^\beta$, with $\tau_{d,160}$ the dust opacity close to the [C II] 158 μm line, and β a grain emissivity index. The resulting L_{FIR} and $\tau_{d,160}$ maps, where we have allowed β to be a free parameter of the fits, are shown in Figures 8(a) and (f). The mean β value is 2.4 ± 0.5 (1σ), but we note that the derived FIR luminosities and dust opacities, the relevant quantities for our analysis, do not change significantly by fixing β to a constant value of 2. We also estimated the pixel-averaged gas column density and mass. In particular, we used the SPIRE 250 μm image assuming that it corresponds to optically thin dust emission and computed the equivalent gas mass per pixel as

$$M_{\text{Gas}} = \frac{R_{\text{gd}} S_{250} D^2}{\kappa_{250} B_{250}(T_d)} \quad (2)$$

(Hildebrand 1983), where S_{250} is the 250 μm flux density within Ω , R_{gd} is the gas-to-dust mass ratio, and κ_{250} is the dust absorption cross section divided by the dust mass. We adopt $R_{\text{gd}}/\kappa_{250} = 25 \text{ gr cm}^{-2}$, computed from grain properties taken from Draine's tabulations (Li & Draine 2001, and references therein) for a grain size distribution that leads to an A_V/N_{H} ratio compatible with observations of Orion (see Section 3.2).

²⁰ The central region of the photometric image (BN/KL outflows and IRc sources) contains saturated data points that are not used in our analysis.

3. RESULTS

3.1. Global Morphology of the [C II] 158 μm Emission

Figure 1 (left) shows a composite image of OMC 1 in the integrated line emission of CO 2–1 (red), [C II] 158 μm (blue), and H41 α (green). This image shows the H II/PDR/molecular gas stratification expected in molecular clouds irradiated by strong UV fields from nearby massive stars.

The H41 α recombination line traces dense ionized gas from the blister H II region surrounding the Trapezium. The H41 α line peaks near the OB stellar cluster and is also bright adjacent to the Orion Bar PDR. Despite the different angular resolutions, the H41 α emission morphology is similar to the brightest regions seen in the visible-light H α images of the Orion Nebula (M42) (Figure 2, left; Robberto et al. 2013).

Figure 3 shows [C II], CO 2–1, and H41 α spectra extracted from representative lines of sight toward OMC 1, namely, the northern streamer, BN/KL, the Trapezium, the Orion Bar, the East PDR, and the extended cloud face in the south. OMC 1 has an overall face-on geometry, with the molecular cloud located ~ 0.3 – 0.6 pc behind the ionizing stars (e.g., Hogerheijde et al. 1995; van der Werf et al. 2013). Therefore, the observed ~ 10 – 15 km s^{-1} blueshift of the H41 α line relative to the [C II] and CO lines (Figure 3) is consistent with streamers of ionized gas escaping from the high-pressure H II/OMC 1 interface and moving toward the observer (e.g., Genzel & Stutzki 1989).

The regions of brightest [C II] 158 μm emission delineate the far edges of the H II blister and follow a roughly spherical shell distribution (as projected in the plane of the sky) with emission peaks near the Trapezium, at the east of BN/KL (which we refer to as the ‘‘East PDR’’) and along the Orion Bar PDR (Figure 1, right). These ‘‘interface’’ regions at the back side of the H II region show very bright [C II] emission, with main-beam temperature peaks of $\gtrsim 150$ K (or a surface brightness of $\gtrsim 5 \times 10^{-3} \text{ erg s}^{-1} \text{ cm}^{-2} \text{ sr}^{-1}$ for the average $\Delta v \simeq 5 \text{ km s}^{-1}$ line width; see Figure 3). In addition, a more extended component of fainter [C II] 158 μm emission exists. In particular, the average line peak temperature in the map is ~ 70 K. This reflects the presence of a lower-density and cooler component, the extended FUV-illuminated ‘‘face’’ of OMC 1 previously detected in [C II] at lower angular and spectral resolutions (Stacey et al. 1993; Herrmann et al. 1997). This extended component is also seen in the wide-field images of M42 taken in the emission from other low ionization potential ($< 13.6 \text{ eV}$) atoms (see the reddish nebular emission in Figure 2 taken with the [S II] filter in the visible). It is also seen in the near-IR vibrationally excited H₂ emission attributed to large-scale FUV fluorescence (Luhman et al. 1994).

Most of the [C II] (and obviously CO) emission is expected to arise from the neutral cloud. This can be readily seen from the similar [C II] 158 μm and CO 2–1 line profiles and also similar line peak velocities (Figure 3). At the small spatial scales revealed by our observations ($\sim 5000 \text{ AU}$), however, both the integrated intensity map (Figure 1, left) and the velocity channel maps (Figure 7) show that the [C II] and CO 2–1 spatial distribution does not exactly match. This is more obvious toward (nearly) edge-on PDRs, like the Orion Bar, because the irradiated cloud edge (emitting [C II]) can be resolved from the more shielded molecular gas, where CO reaches its abundance peak ($A_V \gtrsim 3 \text{ mag}$ for dense gas and strong FUV fields; see the representative model in Figure 5).

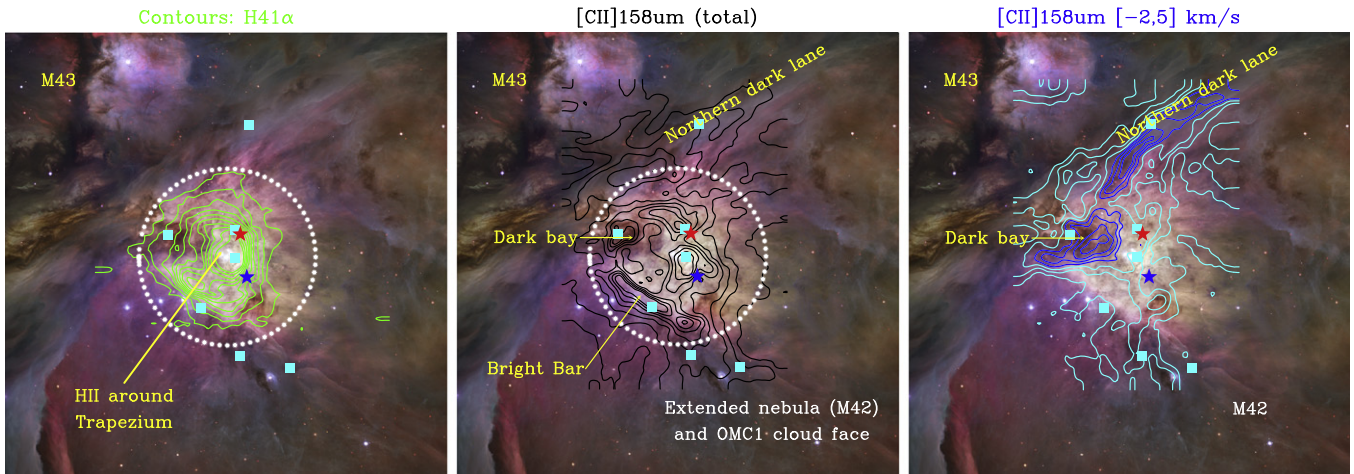


Figure 2. Color-composite visible image of the Orion Nebula (M42) taken with the ACS instrument on board the *Hubble Space Telescope* (*HST*). The assigned colors are: red and orange for [S II] and H α , blue for *B*, and green for *V* filters (Robberto et al. 2013). *Left*: Green contours show the integrated intensity (W) of the H41 α recombination line (from 3 to 21 K km s $^{-1}$ in steps of 2 K km s $^{-1}$). The white dotted 200'' (0.4 pc) radius circle is centered on θ^1 Ori C, the brightest star of the Trapezium. We define the “extended cloud face” component to lie outside this circle. *Middle*: black contours show the total [C II] 158 μ m integrated intensity ($v_{\text{LSR}} = -30$ to +30 km s $^{-1}$ with W from 0 to 1300 K km s $^{-1}$ in steps of 150 K km s $^{-1}$). *Right*: [C II] “blueshifted streamer” (emission from $v_{\text{LSR}} = -2$ to +5 km s $^{-1}$) with W from 0 to 60 K km s $^{-1}$ (cyan) and from 80 to 140 K km s $^{-1}$ (blue), all in steps of 20 K km s $^{-1}$. This emission coincides with the *Northern Dark Lane* and with the *Dark Bay* seen in visible-light images of the nebula. The Orion hot core in the BN/KL region and Orion S positions are indicated by red and blue stars, respectively. The positions where line spectra have been extracted (shown in Figure 3) are indicated by cyan squares.

The integrated intensity maps also reveal regions of moderately bright [C II] 158 μ m emission, but a very weak CO emission counterpart (northeastern areas). In addition, they show regions, such as the shocked gas toward H $_2$ Peaks 1 and 2 in Orion BN/KL outflows, where the CO line luminosities are exceptionally high (see also Goicoechea et al. 2015).

Finally, Figure 4 shows the good spatial correspondence between the [C II] 158 μ m integrated intensity (contours) and the *Spitzer*/IRAC 8 μ m emission (e.g., Megeath et al. 2012). This image is dominated by fluorescent IR emission from PAHs (after absorption of UV photons; e.g., Allamandola et al. 1989) and by very small grain emission, with minor contribution from [Ar III] toward the H II region and from H $_2$ lines toward particular positions of enhanced shocked gas emission (Rosenthal et al. 2000).

3.2. Template Regions and Representative PDR Model

Based on our knowledge of Orion (e.g., Genzel & Stutzki 1989; Stacey et al. 1993; Bally 2008), and in order to ease the interpretation of the [C II] and related maps, we introduce three different regions (or sightlines). We first consider a 200'' (0.4 pc) radius circle centered on θ^1 Ori C, the brightest star of the Trapezium (e.g., the white dotted circle shown in Figure 4). We define the “extended cloud face” component for positions outside this circle. Second, a small $R < 0.1$ pc circle around the Trapezium defines lines of sight that go through the “H II region” component around the H41 α emission peak. Finally, we consider a spherical shell, or annulus, delineated by the $R = 0.16$ pc and $R = 0.24$ pc circles. This region represents “PDR interfaces” between OMC 1 and the H II region close to the Trapezium. These PDRs (including the Bar) show a more edge-on configuration and are illuminated by the strong, almost unattenuated, UV field from the Trapezium stars.

To guide our interpretation, Figure 5 shows the predicted structure of the H/H $_2$ and C $^+$ /C/CO transitions as a function of visual extinction (A_V) for physical conditions ($G_0 = 2 \times 10^4$ and $n_{\text{H}} = 2 \times 10^5$ cm $^{-3}$) representative of the H II/OMC 1

interface near the Trapezium (see Section 4). This homogeneous, stationary slab cloud model was computed with the *Meudon* PDR code (Le Petit et al. 2006). We adopted [C/H] = 1.4×10^{-4} (from *Hubble Space Telescope* absorption observations toward the star HD 37021 in the Trapezium; Sofia et al. 2004) and a flat extinction curve compatible with observations of Orion (Lee 1968; Cardelli et al. 1989; Allers et al. 2005; Abel et al. 2006). In particular, an extinction-to-color-index ratio ($R_V = A_V/E_{B-V}$) of 5.5 and $A_V/N_{\text{H}} = 3.5 \times 10^{-22}$ mag cm $^{-2}$ were adopted. These values are different from the standard grain properties used in diffuse cloud models ($R_V = 3.1$ and $A_V/N_{\text{H}} = 5.3 \times 10^{-22}$ mag cm $^{-2}$) and are consistent with larger-than-standard-size grains in Orion. Larger grains lead to an increased penetration of FUV photons, larger size of the C $^+$ zone ($\Delta A_V(\text{C}^+) \gtrsim 1$ mag), higher C $^+$ column densities, and shift the peak CO formation layer to larger A_V deeper inside the cloud (see also Goicoechea & Le Boulrot 2007).

More in general, an ionization front can move into the molecular cloud. Ionized gas will rapidly photoevaporate from the cloud surface, and the PDR structure will not be in equilibrium (e.g., Bertoldi & Draine 1996). Thus, dynamical effects might alter the picture shown in Figure 5. Non-stationary PDR models predict that a well-defined C $^+$ /CO transition layer always exists, although the layer is slightly shifted closer to the cloud surface (by only $\Delta A_V \simeq 0.5$ for G_0/n_{H} conditions appropriate to OMC 1) owing to advection of CO from inside the cloud (Störzer & Hollenbach 1998). Since the predicted C $^+$ column density in these models does not vary much compared to that in stationary models, the general predictions shown in Figure 5 for C $^+$ should remain valid.

3.3. Kinematics: [C II] 158 μ m Velocity Channel Maps

Figures 6 and 7 show continuum-subtracted [C II] 158 μ m velocity channel maps compared to those of H41 α and CO 2–1 lines, respectively. Both figures show the emission in 1 km s $^{-1}$

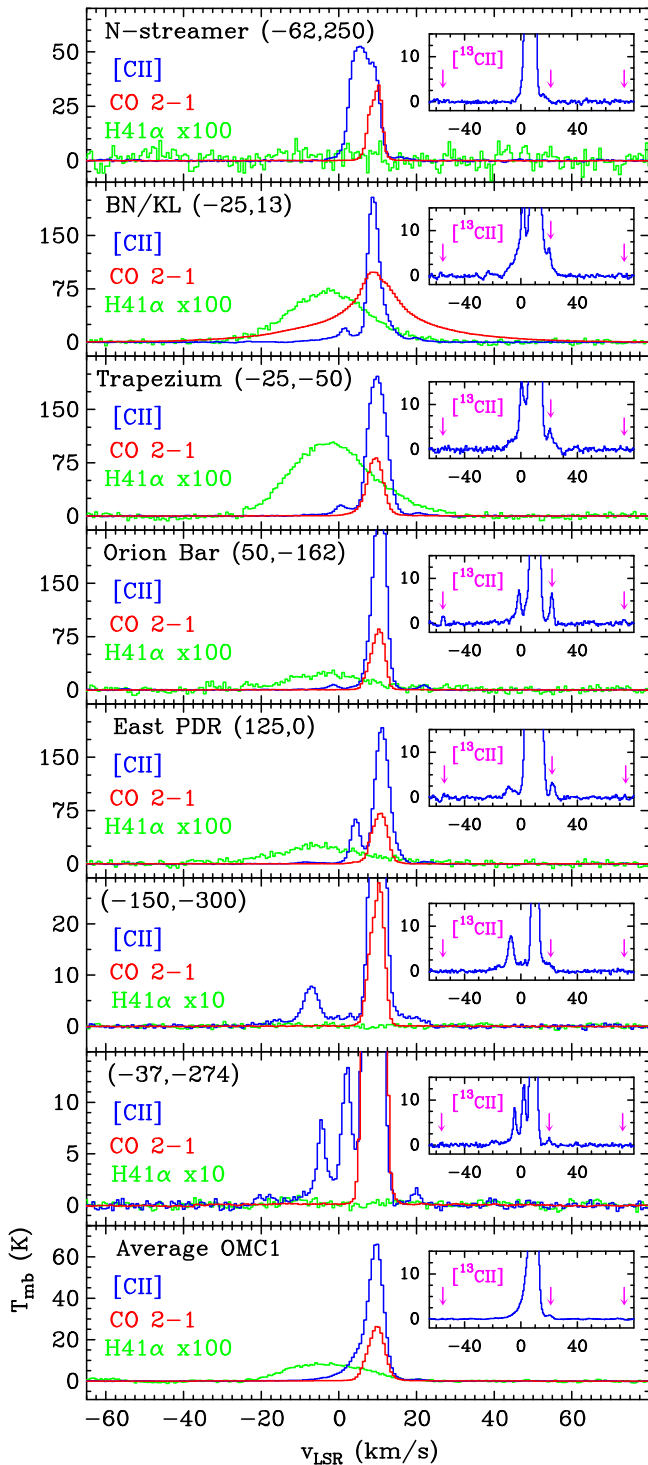


Figure 3. [C II] 158 μm , CO 2-1, and H41 α line profiles toward representative positions in Orion. Offsets in arcsec are given with respect to the HIFI map center at α_{2000} : $5^{\text{h}}35^{\text{m}}17^{\text{s}}.0$, δ_{2000} : $-5^{\circ}22'33''.7$. The last panel shows the average spectrum over the region. The inset panels show a zoom into the spectra. The magenta arrows mark the expected positions of the [$^{13}\text{C II}$] $F=1-0$, $2-1$, and $1-1$ hyperfine components (from left to right). The [C II] and CO spectra were extracted from maps convolved to $25''$ resolution.

velocity channels from $v_{\text{LSR}} = -9$ to $+20$ km s^{-1} ([C II] 158 μm in colored maps and H41 α or CO 2-1 lines in white contours). They reveal the intricate small spatial scale kinematics of the ionized/PDR/molecular gas interfaces.

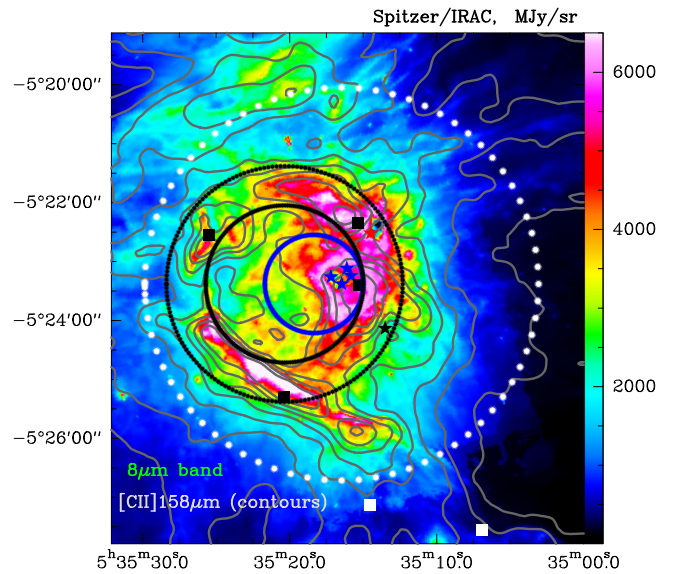


Figure 4. Spitzer/IRAC 8 μm filter image (dominated by PAH emission) toward OMC 1. Contours show the total [C II] 158 μm integrated intensity (from 0 to 1300 K km s^{-1} in steps of 150 K km s^{-1}). The different circles and regions are defined in Section 3.2. The positions where line spectra have been extracted (shown in Figure 3) are indicated by squares.

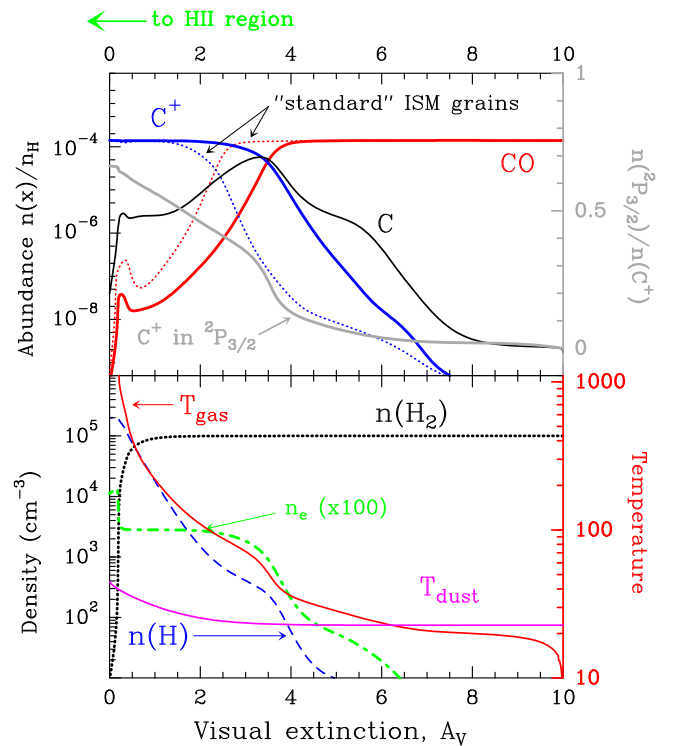


Figure 5. H $_2$ and C $^+$ /C/CO transitions predicted by the Meudon PDR code for physical conditions and grain properties representative of OMC 1 near the Trapezium cluster ($G_0 = 2 \times 10^4$ and $n_{\text{H}} = n(\text{H}) + 2 n(\text{H}_2) = 2 \times 10^5 \text{ cm}^{-3}$). The equivalent length of the $A_V = 10$ mag slab is $\approx 10,000$ AU ($\approx 24''$ at the distance to OMC 1). The dotted C $^+$ and CO abundance profiles in the upper panel are obtained using standard, diffuse ISM, grain properties (see Section 3.2).

The velocity centroid of the molecular cloud emission,²¹ traced by CO, lies at $v_{\text{LSR}} \approx +(8-10) \text{ km s}^{-1}$. The [C II]

²¹ The Orion A molecular complex to which OMC 1 belongs shows a velocity gradient of $0.7 \text{ km s}^{-1} \text{ pc}^{-1}$ over ~ 25 pc (e.g., Bally et al. 1987).

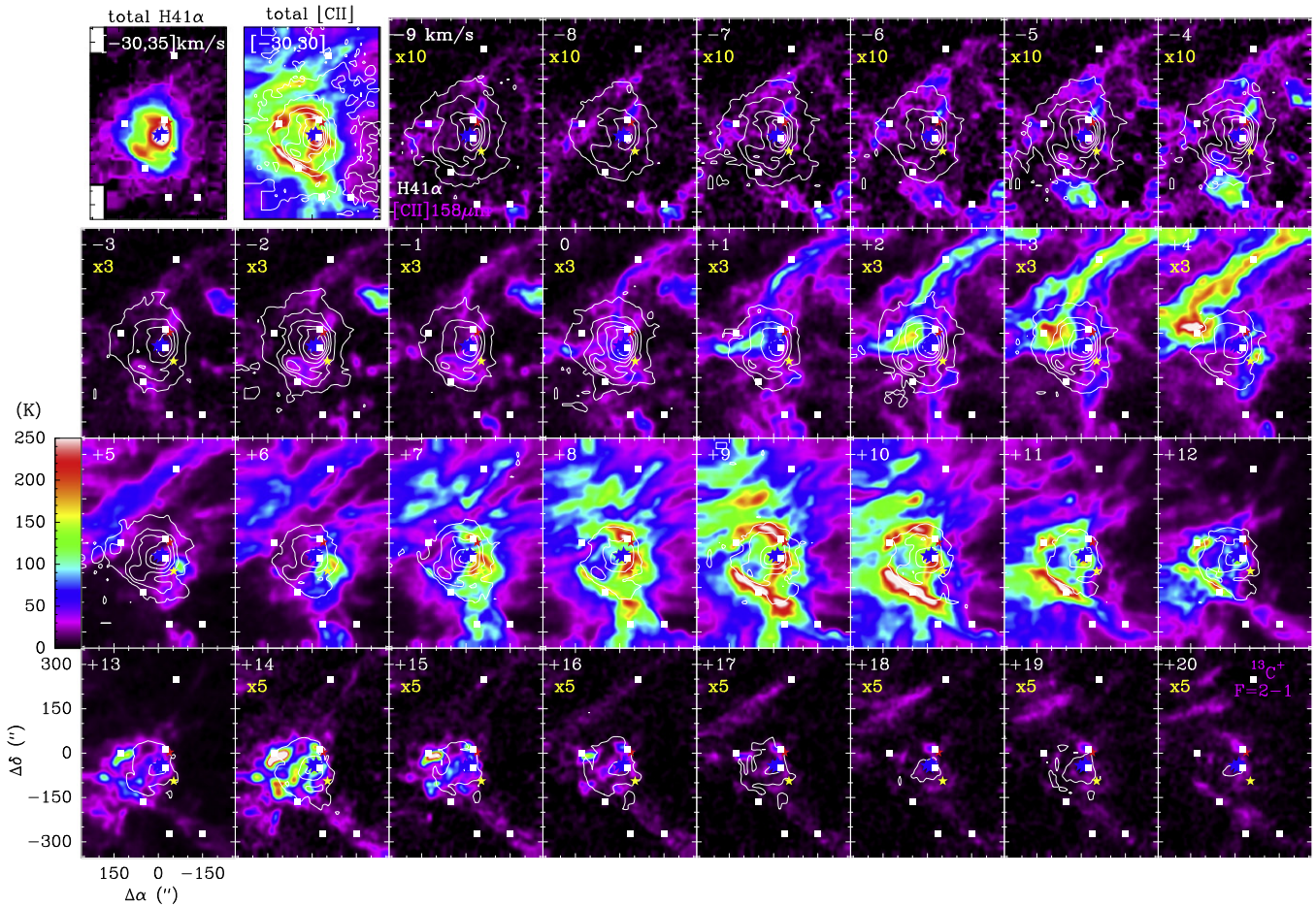


Figure 6. Velocity channel maps in steps of 1 km s^{-1} from $v_{\text{LSR}} = -9$ to $+20 \text{ km s}^{-1}$ ([C II] in colors and H41 α line in contours). The [C II] main-beam temperature scale in bins of 1 km s^{-1} is given in the color wedge (in some velocity intervals the [C II] intensity per channel is multiplied by a factor that is specified in each panel). Offsets in arcsec are given with respect to the HIFI map center. The H41 α contours go from 0.2 to 1.8 K km s^{-1} in steps of 0.3 K km s^{-1} . The [C II] emission seen at $v_{\text{LSR}} = +20 \text{ km s}^{-1}$ (last panel) is dominated by the $^{13}\text{C II} F = 2-1$ line peak. Note that the first two upper-left panels show total integrated line intensity maps for H41 α (from 0 to 22 K km s^{-1}) and [C II] $158 \mu\text{m}$ (from 0 to 1300 K km s^{-1}). In the total [C II] intensity map, H41 α integrated line intensities are shown as white contours (from 1 to 21 K km s^{-1} in steps of 4 K km s^{-1}). The Orion hot core, Orion S condensation, and Trapezium stars are indicated by red, yellow, and blue stars, respectively. The positions where line spectra have been extracted (shown in Figure 3) are indicated by white squares.

$158 \mu\text{m}$ spectrum average over all mapped positions is characterized by a very bright component peaking at $v_{\text{LSR}} \simeq +9.5 \text{ km s}^{-1}$, with a line-width of $\sim 5 \text{ km s}^{-1}$ (lowest panel in Figure 3), in agreement with CO velocity and line widths.

This emission mostly arises from the H II/OMC 1 interfaces close to the Trapezium (inside the $200''$ radius circle) and also from the large-scale FUV-illuminated face of the molecular cloud (outside). Therefore, the main [C II] spectral component that coincides with CO ($v_{\text{LSR}} \sim 5\text{--}17 \text{ km s}^{-1}$) is dominated by C⁺ in dense PDR gas and represents $\sim 85\%$ of the total [C II] luminosity in the map. The emission is so bright that the $^{13}\text{C II} F = 2-1$ line, the strongest $^{13}\text{C II}$ hyperfine component (Ossenkopf et al. 2013), is also detected toward the highest column density peaks (see the inset in Figure 3 and the channel maps between $+17$ and $+20 \text{ km s}^{-1}$ in Figures 6 and 7).

Other specific regions such as the Orion Bar PDR show [C II] line peak velocities at $v_{\text{LSR}} \simeq +(10\text{--}12) \text{ km s}^{-1}$ and thus have a slightly differentiated kinematics. In fact, [C II] shows widespread emission in a broad range of velocities outside the main spectral component range. On the other hand, the CO 2-1 emission range is much more restricted, with the high velocity CO emission seen at $v_{\text{LSR}} < 0 \text{ km s}^{-1}$ and $v_{\text{LSR}} >$

15 km s^{-1} being very localized, and mostly arising from the molecular outflows surrounding Orion BN/KL and S.

Despite the relatively flat [C II] intensity distribution suggested by previous lower-resolution observations, the [C II] channel maps show complicated structures and velocity patterns. This is true even away from the Trapezium, where filamentary structures and emission striations are seen at several velocity intervals. At the $v_{\text{LSR}} \approx +8\text{--}10 \text{ km s}^{-1}$ velocity of the neutral cloud, the H41 α emission delineates the far edges of the expanding H II blister in close interaction with the cloud. This produces a bright shell-shaped [C II] emission from compressed PDRs immediately beyond the ionization fronts. This is the signature of the UV radiation *eating into* the cloud.

Also at $v_{\text{LSR}} \approx +8\text{--}10 \text{ km s}^{-1}$, but away from the H II region, [C II] shows narrow striations or sheet-like structures that are roughly perpendicular to the main molecular ridge (north to south) and do not show much CO emission. As suggested by the overlap with the visible-light images of M42 (Figure 2), these photoevaporative [C II] structures demonstrate that the entire field and velocity range is permeated by FUV photons.

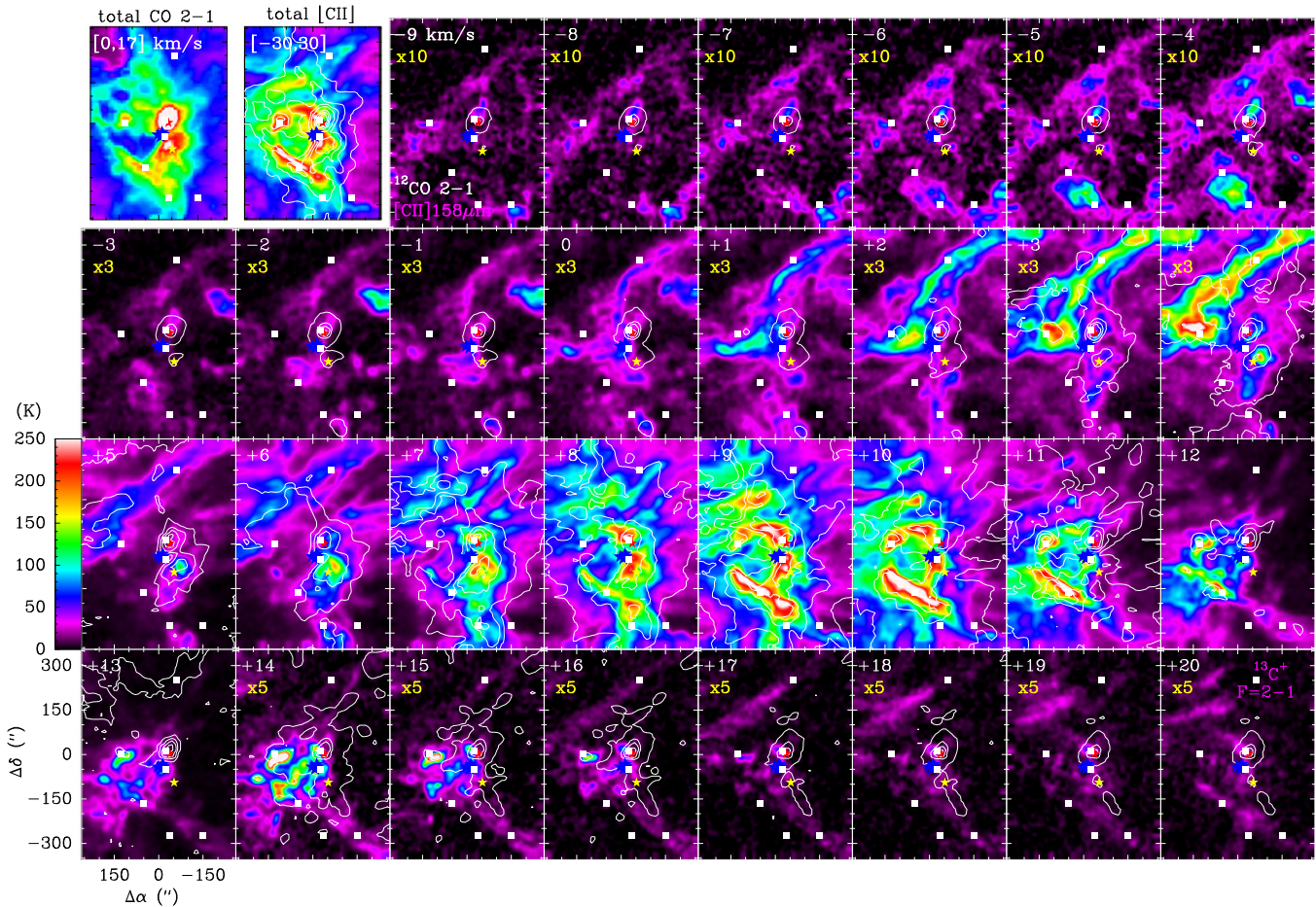


Figure 7. Same as Figure 6 but the CO 2–1 line (in contours). The CO 2–1 contours go from 1.5 to 160 K km s^{−1} in steps of 30 K km s^{−1}. The high-velocity CO 2–1 emission ($v_{\text{LSR}} < 0$ s^{−1} and $v_{\text{LSR}} > 15$ s^{−1}) mostly arises from molecular outflows around Orion BN/KL and Orion S protostellar sources. At other positions, the observed [C II] emission in these velocity ranges does not have a CO emission counterpart (e.g., the blueshifted [C II] streamer at $v_{\text{LSR}} = -2$ to $+5$ km s^{−1}, or the [C II] emission in the southwest at $v_{\text{LSR}} \gtrsim 12$ km s^{−1} beyond the Orion Bar). The first two upper-left panels show total integrated line intensity maps of CO 2–1 (from 0 to 600 K km s^{−1}) and [C II] 158 μm (from 0 to 1300 K km s^{−1}). In the [C II] total intensity map, CO 2–1 integrated line intensities are shown as white contours, from 200 to 500 K km s^{−1} in steps of 100 K km s^{−1} (extended emission) and from 800 to 1400 K km s^{−1} in steps of 200 K km s^{−1} (Orion BN/KL outflows).

The most negative velocities show H41α emission around the Trapezium. This is probably the edge of the H II blister that is expanding toward the observer. The analogous [C II] emission has some spatial correspondence, but it also shows specific blueshifted structures that do not follow the H41α emission and that must lie in the line of sight toward OMC 1.

3.3.1. C⁺ Gas with No CO Counterpart

In certain velocity ranges the observed [C II] emission does not have any CO emission counterpart. The most outstanding structure with no, or very little, CO emission is a blueshifted [C II] emission “streamer” ($v_{\text{LSR}} = -2$ to $+5$ km s^{−1}) that goes north of Orion BN/KL and also a compact region that fills the cavity inside the bright [C II] shell-like structure (Figure 2). These structures are not coincident with H41α emission tracing H II gas, suggesting that they arise from warm neutral gas of low shielding ($A_V \approx 0$ –4 mag), in which very little or no CO exists (owing to the elevated FUV field in the region and thus rapid photodissociation). Interestingly, they do coincide with foreground depressions of the visible-light emission known as the *Dark Bay* and the Northern Dark Lane that separates M42 and M43 nebulae (blue contours in Figure 2, right).

The column density of material in these structures is sufficient to have significant hydrogen in molecular form (consistent with the detection of radio OH lines in absorption toward the Dark Bay region, e.g., Brogan et al. 2005). Hence, they can be referred to as CO-dark H₂ gas (Grenier et al. 2005; Wolfire et al. 2010), which can also be detected by dust extinction of visible light (O’Dell & Yusef-Zadeh 2000). In [C II] emission, they represent large-scale structures of C⁺ gas surrounding OMC 1 and showing blueshifted velocities relative to the molecular cloud (dark blue contours in Figure 2, right). In terms of luminosity, the [C II] emission from $v_{\text{LSR}} \approx -2$ to $+5$ km s^{−1}, not related to OMC 1, accounts for $\sim 12\%$ of the total [C II] luminosity.

Surprisingly, the [C II] line shows emission components at even more negative LSR velocities throughout the region, in particular in the $v_{\text{LSR}} \approx -10$ to -2 km s^{−1} range, and a fainter blue emission wing at $v_{\text{LSR}} \approx -25$ to -10 km s^{−1} (see spectra in Figure 3). Their combined contribution to the total [C II] luminosity is, however, small, $\sim 3\%$.

Some of the structures showing [C II] emission but no CO counterpart can be associated, both spatially and in velocity space, with particular regions of H I absorption observed against the radio continuum. They are produced by the “Veil,” a collection of absorbing H I layers in the line of sight toward

Orion with little H_2 , less than one part in 10^6 (Troland et al. 1989; Abel et al. 2006). For a detailed explanation of the different H I absorbing velocity components (A, B, C, D ...) see, e.g., van der Werf et al. (2013). In particular, components A and B of the H I absorption maps produce strong H I opacity in the $v_{\text{LSR}} \simeq 0$ to $+6 \text{ km s}^{-1}$ range. Components A and B are interpreted as a foreground veil of nearly atomic gas in front of the Orion Nebula. Thus, the [C II] emission in the $v_{\text{LSR}} \simeq 0$ to $+6 \text{ km s}^{-1}$ range, and outside the Dark Bay and North Dark Lane regions, likely arises from these neutral atomic layers of the Veil (cyan contours in Figure 2, right).

Component C of the H I absorption (from $v_{\text{LSR}} \simeq -4$ to -2 km s^{-1}) is only found at the southwestern edge of OMC 1, and we also detect [C II] emission at those velocities and positions. Finally, H I absorption components D1 and D2 near the Bar appear in the $v_{\text{LSR}} \simeq -20$ to -10 km s^{-1} range and are interpreted as an expanding shell of atomic gas (van der Werf et al. 2013). The most blueshifted [C II] emission ($v_{\text{LSR}} < -10 \text{ km s}^{-1}$) is detected toward the southern regions of the map. Hence, part of this [C II] emission may arise from D1 and D2. In addition, a fraction of this blueshifted [C II] emission may arise from the foreground H II region that lies between the Veil and the Trapezium, and that is not the main H II region interacting with OMC 1. The [N II] $\lambda 6585$ emission line and P III $\lambda 1335$ and S III $\lambda 1190$ absorption lines centered at $v_{\text{LSR}} < -13 \text{ km s}^{-1}$ arise from this foreground H II region (e.g., Abel et al. 2006). Unfortunately, the sensitivity of our [C II] observations is insufficient to map these faint features and to determine a definite association.

H I emission tracing denser gas associated with the molecular cloud is detected at $v_{\text{LSR}} > +10 \text{ km s}^{-1}$, outside the strong H I absorption range of the Veil. Indeed, we find specific regions that show coincident [C II] and H I redshifted emission. The brightest one is the Orion Bar, where both [C II] and H I trace the most exposed PDR layers, in which H_2 is photodissociated. In addition, an elongated [C II] and H I emission feature without a CO counterpart ($v_{\text{LSR}} \gtrsim +12 \text{ km s}^{-1}$) extends in the southwest direction beyond the Bar and along the Bar prolongation seen at visible wavelengths (Figure 2). Another remarkable emission feature is the high-velocity [C II] and H I line wing detected toward Orion BN/KL outflows. Its presence confirms that the shocked material is illuminated by FUV radiation (Chen et al. 2014; Goicoechea et al. 2015).

All in all, our observations demonstrate the link between [C II] and both H I absorption (hydrogen mostly atomic gas) and H I emission (hydrogen predominantly molecular). In particular, $\sim 15\%$ of the total [C II] luminosity does not have a CO counterpart. Most arises from cold H I gas and from CO-dark H_2 gas (e.g., the Dark Bay), but also from H II gas. The contribution from ionized gas is expected to decrease with increasing electron density (n_e) and effective temperature (T_{eff}) of the ionizing stars (as carbon becomes doubly ionized). Both quantities are high toward the Trapezium, $T_{\text{eff}} \simeq 39,000 \text{ K}$ for the θ^1 Ori C star (Simón-Díaz et al. 2006) and $\langle n_e \rangle \simeq (0.5-1) \times 10^4 \text{ cm}^{-3}$ in the surrounding H II region (Zuckerman 1973). For these conditions, models predict that the contribution of [C II] from ionized gas is small, of the order of $\lesssim 10\%$ of the PDR plus H II emission (Abel 2006a). This agrees with our general conclusion that most of the observed [C II] luminosity in Orion arises from dense PDR gas.

3.3.2. [C II] Line Broadening and C^+ Gas Turbulence

The [C II] $158 \mu\text{m}$ line width of the main spectral component varies from $\Delta v_{\text{FWHM}} \sim 3.5 \text{ km s}^{-1}$ toward the extended “face” of OMC 1, to $\sim 4.0 \text{ km s}^{-1}$ toward the Orion Bar, to $\sim 5.5 \text{ km s}^{-1}$ toward the Trapezium. The two latter values are likely affected by opacity broadening (see Section 4.1 for a determination of [C II] opacities). In particular, for $\tau_{[\text{C II}]} \simeq 1-3$, opacity broadening increases the line widths by $\sim 10\%-30\%$ (e.g., Phillips et al. 1979; Ossenkopf et al. 2013). We note that the line widths of the C91 α radio recombination line toward the Orion Bar are $2.0-2.5 \text{ km s}^{-1}$ (Wyrowski et al. 1997).

In the dense PDR gas traced by the [C II] main spectral component inside the $200''$ radius circle, the gas temperature is $T_k \simeq 300-1000 \text{ K}$ (see Figure 5 and Section 4.1.1), implying a thermal broadening of $\sigma_{\text{th}} = (kT_k/m_{\text{C}^+})^{1/2} \simeq 0.5-0.8 \text{ km s}^{-1}$. The nonthermal velocity dispersion σ_{turb} (from turbulence and macroscopic motions) is $\sigma_{\text{turb}} = (\sigma^2 - \sigma_{\text{th}}^2)^{1/2}$, where $\sigma = \Delta v_{\text{FWHM}}/2.355$. For the above line widths and gas temperatures, one obtains $\sigma_{\text{turb}} = 1.2-1.7 \text{ km s}^{-1}$ (after opacity broadening correction). This has to be compared with the isothermal sound speed in the warm PDR gas, $c_{\text{PDR}} = (kT_k/m)^{1/2} \simeq 1.4-3.0 \text{ km s}^{-1}$ (with m the mean mass per atom). In other words, the nonthermal velocity dispersion in the dense PDR gas is subsonic or only weakly supersonic (with Mach numbers $\sigma_{\text{turb}}/c_{\text{PDR}}$ of $\simeq 0.4-1.2$).

In the intermediate $v_{\text{LSR}} = -2$ to $+5 \text{ km s}^{-1}$ components, the [C II] line is narrower, for example, $\Delta v_{\text{FWHM}} \sim 2.5-3.0 \text{ km s}^{-1}$ toward the blueshifted streamer that coincides with the North Dark Lane. On the other hand, the most blueshifted [C II] component with neither a CO nor H41 α counterpart, for example, the features at $v_{\text{LSR}} \simeq -7 \text{ km s}^{-1}$ toward ($-150''$, $-300''$) or at $v_{\text{LSR}} \simeq -5 \text{ km s}^{-1}$ toward ($-37''$, $-274''$), show again broader line widths of $\Delta v_{\text{FWHM}} \sim 4.7 \text{ km s}^{-1}$ (Figure 3). Assuming optically thin [C II] emission and $T_k < 300 \text{ K}$, we find an increased $\sigma_{\text{turb}} \simeq 2 \text{ km s}^{-1}$ (or $\sigma_{\text{turb}}/c_{\text{HI}} > 2$) in these CO-dark components surrounding OMC 1. These results suggest that the gas turbulence is more strongly dissipated in the dense H II/OMC 1 interfaces than in the surrounding, more turbulent, halo components.

3.4. Surface Luminosity Maps

Figure 8 shows maps of different luminosity²² and luminosity ratios that are often discussed in the context of star formation and galaxy properties (e.g., Carilli & Walter 2013).

3.4.1. Dust Opacity, Mass, and Surface Density

Figure 8(a) shows a map of L_{FIR} per pixel obtained by integrating the dust SED¹⁹ fits at each position. Despite the relatively small area covered ($\sim 1.25 \text{ pc}^2$), the FIR intensity exhibits variations of ~ 3 orders of magnitude (excluding Orion BN/KL). L_{FIR} is obviously high toward the high column density²³ regions in the molecular ridge ($N_{\text{H}} \gtrsim 10^{23} \text{ cm}^{-2}$), and locally, it reaches even higher values toward the embedded star-forming cores in Orion BN/KL. Figure 8(f) shows a map of the dust opacity ($\tau_{\text{d},160}$) from Equation (1) for each line of sight. The observations reveal moderate FIR opacities toward Orion S and along the molecular ridge ($\tau_{\text{d},160} \approx 0.2$). The FIR

²² Line luminosity per pixel integrating all [C II] spectral components.

²³ Using $N_{\text{H}}(\text{cm}^{-2}/\text{pixel}) = N(\text{H}) + 2N(\text{H}_2) = M_{\text{Gas}}/(\mu m_{\text{H}} D^2 \Omega)$, with M_{Gas} obtained from Equation (2).

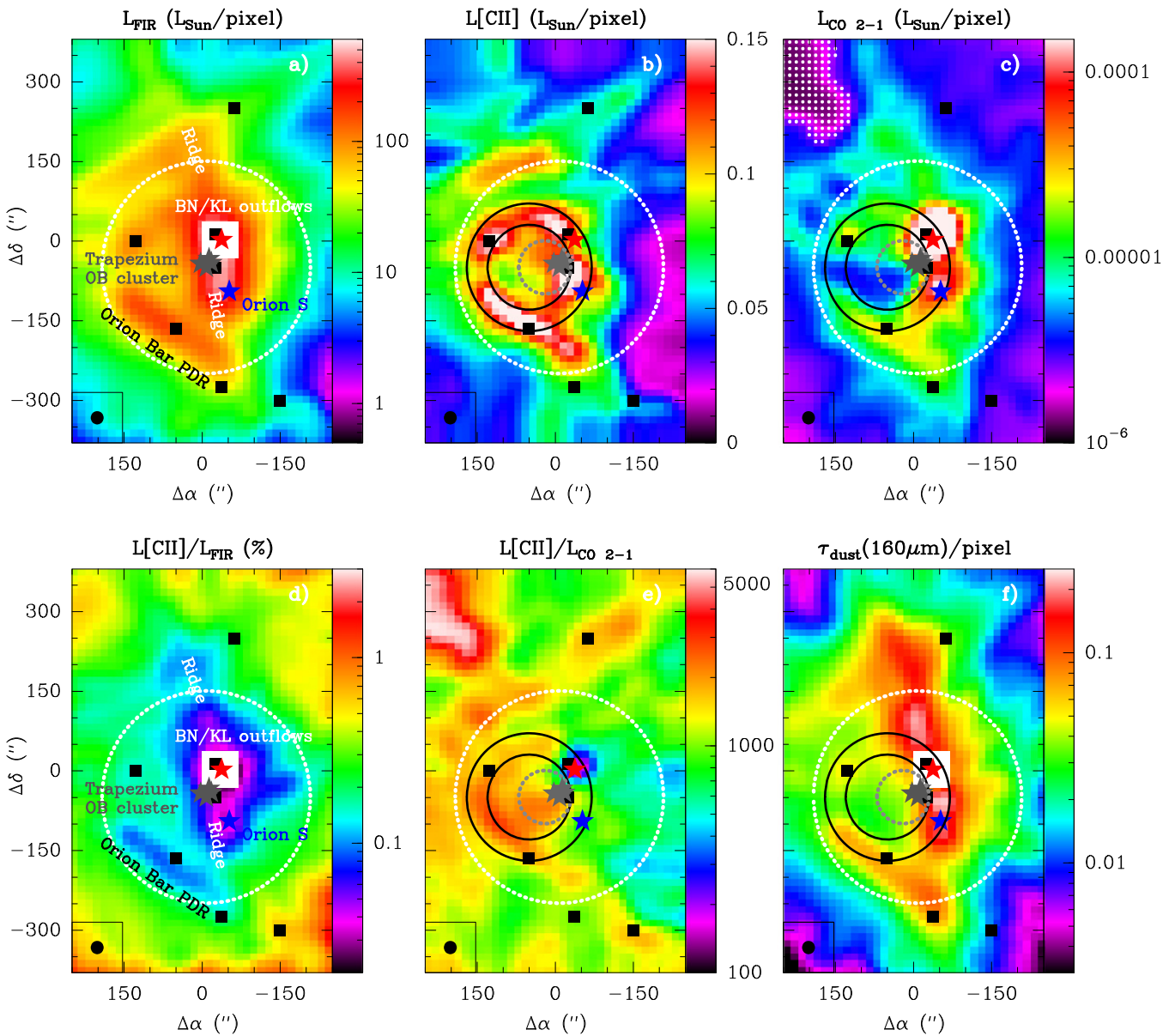


Figure 8. Luminosity and dust opacity per pixel map toward OMC 1 convolved to $25''$ resolution. (a) L_{FIR} map ($G_0 \approx 200 L_{\text{FIR}}/L_{\odot}$ per pixel; see footnote 24), (b) $L[\text{C II}]$, (c) $L_{\text{CO } 2-1}$ (from Berné et al. 2014), (d) $L[\text{C II}]/L_{\text{FIR}}$ in %, (e) $L[\text{C II}]/L_{\text{CO } 2-1}$, and (f) dust opacity at $160 \mu\text{m}$ from SED fits. The white squares in panel (c) represent positions of low $L_{\text{CO } 2-1}$ and high $L[\text{C II}]/L_{\text{CO } 2-1}$ ratios (up to ~ 5000) in panel (e); see also Figure 12. The different circles and regions are defined in Section 3.2. The black squares indicate the positions of the spectra shown in Figure 3. The white square areas in the central BN/KL region indicate positions where the *Herschel* photometric observations are saturated.

opacity then decreases from the Bar ($\tau_{\text{d},160} \lesssim 0.1$) to the extended regions ($\tau_{\text{d},160} \approx 0.01$). Note that the $160 \mu\text{m}$ dust emission toward Orion BN/KL is optically thick ($\tau_{\text{d},160} > 1$; Goicoechea et al. 2015; and Section 5.4.1).

The total gas mass in the mapped region is computed from the optically thin dust emission at $250 \mu\text{m}$ using Equation (2). For the assumed grain properties (see Section 3.2), we derive $M_{\text{Gas,Total}} \simeq 2600 M_{\odot}$ in the $\sim 0.9 \text{ pc} \times 1.4 \text{ pc}$ mapped area (excluding Orion BN/KL, which adds $\sim 100 M_{\odot}$; Goicoechea et al. 2015). This is equivalent to a surface density of $\Sigma_{\text{Gas}} \simeq 2000 M_{\odot} \text{ pc}^{-2}$. We note that an $R_{\text{gd}}/\kappa_{250}$ ratio higher than the assumed in this work will increase our gas mass estimate and the N_{H} -to- A_{V} conversion value accordingly. Unfortunately, the exact grain composition and optical properties in molecular clouds like OMC 1 are not fully constrained (Goldsmith et al. 1997), and they likely change on small scales

(Arab et al. 2012). Owing to the similar gas masses reported from large-scale ^{13}CO and submillimeter continuum mapping (Bally et al. 1987; Lis et al. 1998; Berné et al. 2014), we estimate that our M_{Gas} and N_{H} values are uncertain by a factor of $\lesssim 2$.

3.4.2. $L[\text{C II}]/L_{\text{FIR}}$ and $L[\text{C II}]/L_{\text{CO } 2-1}$ Maps

Figure 8(d) shows the spatial distribution of the $L[\text{C II}]/L_{\text{FIR}}$ luminosity ratio toward OMC 1. $L[\text{C II}]/L_{\text{FIR}}$ varies from the more extended and translucent cloud component, where $N_{\text{H}} \approx 10^{21-22} \text{ cm}^{-2}$ and $L[\text{C II}]$ carries up to $\sim 1\%$ – 5% of the FIR luminosity, to the dense molecular ridge, where $N_{\text{H}} \approx 10^{24} \text{ cm}^{-2}$ and $L[\text{C II}]$ only carries $\sim 0.01\%$. The mean (median) value in the map is $L[\text{C II}]/L_{\text{FIR}} = 3.8(2.9) \times 10^{-3}$. This is similar to the value observed toward translucent clouds of the

Table 2
Average Physical Parameters toward Different Regions of OMC 1

	$L[\text{C II}]/L_{\text{FIR}}$	$L_{\text{CO } 2-1}/L_{\text{FIR}}$	$L[\text{C II}]/L_{\text{CO } 2-1}$	$L_{\text{FIR}}/M_{\text{Gas}}$ (L_{\odot}/M_{\odot})	G_0^b (Habing Field)	$\tau_{\text{d},160}$
OMC 1 (full map ^a)	$3.8(5.4) \times 10^{-3}$	$3.6(6.2) \times 10^{-6}$	1200(900)	43(27)	7.5×10^3	0.03(0.03)
Extended Cloud ($R > 0.4$ pc)	$4.7(6.0) \times 10^{-3}$	$4.5(7.5) \times 10^{-6}$	1400(900)	35(20)	3.2×10^3	0.02(0.02)
Dense PDR interface ($0.16 < R < 0.24$ pc annulus ^a)	$1.1(0.5) \times 10^{-3}$	$6.6(2.2) \times 10^{-7}$	1600(500)	87(24)	3.3×10^4	0.08(0.05)
Toward H II around Trapezium ($R < 0.1$ pc)	$9.3(3.9) \times 10^{-4}$	$5.4(1.8) \times 10^{-7}$	1700(400)	126(18)	3.3×10^4	0.05(0.02)

Notes. Average values over the different *template* cloud regions defined in Section 3.2. Numbers in parentheses represent the standard deviation (1σ) of each sample. L_{FIR} refers to the 40–500 μm range.

^a The central Orion BN/KL region ($50'' \times 50''$) is not included in the computation of the average values owing to saturation of the photometric measurements. A low $L[\text{C II}]/L_{\text{FIR}} \simeq (2-8) \times 10^{-5}$ luminosity ratio and $\tau_{\text{d},160} \simeq 1-3$ was inferred from *Herschel*/PACS spectroscopic observations (Goicoechea et al. 2015). The mean $L[\text{C II}]/L_{\text{CO } 2-1}$ ratio in this region is ~ 270 . ^b Estimated from I_{FIR} and Equation (3).

Galaxy (Ingalls et al. 2002). Indeed, low angular resolution surveys of the Milky Way show that the typical $L[\text{C II}]/L_{\text{FIR}}$ ratio in regions of weak [C II] emission is $\sim 4 \times 10^{-3}$, and is decreases to $\sim 10^{-3}$ toward star-forming regions where the [C II] line is brighter (e.g., Nakagawa et al. 1998).

The L_{FIR} map per pixel in Figure 8(a) can be used to estimate, to first order, the spatial distribution of G_0 . Assuming that at large scales the entire column density of dust is heated by absorption of FUV photons, dust grains re-radiate in the FIR at a characteristic temperature ($\approx T_{\text{d}}$), and

$$G_0 \approx \frac{1}{2} \frac{I_{\text{FIR}} (\text{erg s}^{-1} \text{cm}^{-2} \text{sr}^{-1})}{1.3 \times 10^{-4}} \quad (3)$$

(see Hollenbach & Tielens 1999), where G_0 is the FUV field in Habing units.²⁴ The factor of 1/2 approximately takes into account the absorption of visible photons by dust. The maximum value near the Trapezium is $G_0 \simeq 10^5$, whereas the lowest values in the mapped area are $G_0 > 500$. The mean value inside the $200''$ radius circle is $G_0 \simeq 2 \times 10^4$ (the G_0 used in the representative PDR models shown in Figure 5). These FUV fluxes are in good agreement with early estimates based on lower angular resolution observations and PDR modeling (e.g., Tielens & Hollenbach 1985b; Stacey et al. 1993).

The [C II] and CO 2–1 luminosities in the observed area are $L[\text{C II}] = 173 L_{\odot}$ and $L_{\text{CO } 2-1} = 0.15 L_{\odot}$. Figure 8(e) shows the $L[\text{C II}]/L_{\text{CO } 2-1}$ map. The spatial distribution is markedly different from that of $L[\text{C II}]/L_{\text{FIR}}$. In particular, the $L[\text{C II}]/L_{\text{CO } 2-1}$ ratio shows differences locally, from a few hundred in the strong outflows around Orion BN/KL to ~ 5000 in the peculiar northeastern positions almost devoid of CO emission (see white marks in the $L_{\text{CO } 2-1}$ map shown in Figure 8(c)). At other positions of the map, the ratio reaches high values (> 1000), because the observations trace either regions of low extinction (i.e., low CO columns) or nearly edge-on PDRs for which the C^+/CO transition is spatially

resolved. Table 2 summarizes the mean values extracted from the maps toward the different regions of the cloud.

4. ANALYSIS

4.1. [C II] 158 μm Excitation and C^+ Column Densities

Collisions with electrons, H atoms, and H_2 molecules contribute to the excitation of the [C II] $^2P_{3/2}-^2P_{1/2}$ fine-structure levels (see discussion by Goldsmith et al. 2012). The critical densities (n_{cr}) for collisions of C^+ with, e , H, and H_2 are $\sim 44 e/\text{cm}^3$ at $T_e = 8000$ K (Wilson & Bell 2002) and ~ 3000 (2400) H/cm^3 (Barinovs et al. 2005) and ~ 4500 (3400) H_2/cm^3 at $T_k = 100$ (500) K (Wiesenfeld & Goldsmith 2014). Owing to the similar collisional rates with H_2 and H, the [C II] excitation in neutral gas is nearly independent of the molecular fraction. As the gas density increases above n_{cr} , the excitation temperature T_{ex} of the $^2P_{3/2}-^2P_{1/2}$ transition tends to thermalize with T_k . For optically thick lines, line trapping further reduces the critical densities, thus reaching thermalization ($T_{\text{ex}} = T_k$) at lower densities. Also for optically thick lines, a strong FIR background with high T_{bg} values increases T_{ex} but reduces the [C II] line intensity.

When $n_{\text{H}} \lesssim n_{\text{cr}}$, the [C II] excitation becomes subthermal ($T_{\text{ex}} < T_k$). If significant C^+ columns of low-density gas exist in front of an FIR continuum source, the [C II] line will be seen in absorption if $T_{\text{ex}} < 91.2/\ln(1 + 91.2/T_c)$ (e.g., Gerin et al. 2015), where $h\nu/k = 91.2$ K is the equivalent temperature at 1900.537 GHz and $T_c = J(T_{\text{bg}}) = 91.2/(e^{91.2/T_{\text{bg}}} - 1)$ is the continuum brightness temperature at 158 μm . [C II] line self-absorptions can also be produced by excitation gradients within the [C II] emitting region (e.g., Plume et al. 2004; Graf et al. 2012).

One potential problem in interpreting the [C II] 158 μm emission is the difficulty inferring the line opacity. Toward many positions, our observations resolve the $[^{13}\text{C II}] F = 2-1$ line²⁵ arising from the main spectral component at $v_{\text{LSR}} \simeq +9.5 \text{ km s}^{-1}$ (see spectra in Figure 3 and maps in

²⁴ At the distance of OMC 1 and considering the pixel size in Figure 8(a), the L_{FIR} scale per pixel is equivalent to $G_0 \approx 200 L_{\text{FIR}}/L_{\odot}$ (per pixel). This relation neglects dust heating by embedded sources. Here we assume that owing to the high FUV field in the region, this extra heating does not dominate at large scales. For the same reason, and owing to the warm dust grain temperatures, we neglect the dust emission at $> 500 \mu\text{m}$ in the G_0 estimation.

²⁵ Corrected line strengths for the $[^{13}\text{C II}] F = 2-1$, 1–0 and 1–1 hyperfine lines at 1900.466, 1900.950 and 1900.136 GHz respectively have been published by Ossenkopf et al. (2013). The relative line strengths are 0.625, 0.250 and 0.125. These are slightly different from those of Cooksy et al. (1986) that were used in the analysis of Stacey et al. (1991b) and Boreiko & Betz (1996), and resulted in $^{12}\text{C}/^{13}\text{C}$ isotopic ratios lower than the usual value of ~ 67 .

the highest-velocity panels of Figures 6 and 7). The second brightest component, the $[^{13}\text{C II}] F = 1-0$ line, is only detected toward a few positions of very bright $[\text{C II}]$ emission (e.g., the Orion Bar and BN/KL; see Figure 3). Assuming that the total integrated intensity of the three $[^{13}\text{C II}]$ lines is $I[^{13}\text{C II}] = I_{F=2-1}/0.625$, one can derive the $[\text{C II}]$ line opacity from²⁶

$$\frac{1 - e^{-\tau_{[\text{C II}]}}}{\tau_{[\text{C II}]}} \simeq \frac{0.625 T_{\text{P}}([^{12}\text{C II}])/T_{\text{P}}([^{13}\text{C II}], F = 2 - 1)}{I[^{12}\text{C}/^{13}\text{C}]} \quad (4)$$

(e.g., Ossenkopf et al. 2013) where $\tau_{[\text{C II}]}$ is the $[\text{C II}]$ 158 μm opacity at line center, T_{P} is the line peak main beam temperature (continuum subtracted), and $I[^{12}\text{C}/^{13}\text{C}]$ is the isotopic ratio (~ 67 in Orion, Langer & Penzias 1990). For optically thick $[\text{C II}]$ 158 μm emission, the excitation temperature (T_{ex}) of the $^2P_{3/2}-^2P_{1/2}$ transition can be computed from

$$T_{\text{ex}} = \frac{91.2}{\ln\left(1 + \frac{91.2}{T_{\text{P}}(^{12}\text{C}^+) + J(T_{\text{bg}})}\right)} \quad (\text{K}). \quad (5)$$

At these FIR wavelengths, the background is dominated by dust emission so that the continuum level adjacent to the $[\text{C II}]$ line, for an equivalent background temperature of 20–35 K, is $T_{\text{c}} = 1-7$ K, roughly the range of continuum levels detected by HIFI. For the main $[\text{C II}]$ 158 μm spectral component we find $T_{\text{P}}(^{12}\text{C}^+) \gg T_{\text{c}}$; thus, the continuum emission has a minor effect on T_{ex} . However, the situation can be different in more extreme and luminous environments.

Once $T_{\text{ex}}(^2P_{3/2}-^2P_{1/2})$ and $\tau_{[\text{C II}]}$ have been determined, the C^+ column density can be computed from

$$N(\text{C}^+) \simeq 1.5 \times 10^{17} \frac{1 + 2 e^{-91.2/T_{\text{ex}}}}{1 - e^{-91.2/T_{\text{ex}}}} \tau_{[\text{C II}]} \times \Delta v_{\text{FWHM}} \quad (\text{cm}^{-2}), \quad (6)$$

where Δv_{FWHM} is the line width in km s^{-1} of an assumed Gaussian line profile. From the $[\text{C II}]$ and $[^{13}\text{C II}]$ spectra averaged over the mapped region (main spectral component) we find $\langle T_{\text{ex}} \rangle \simeq 100$ K, $\langle \tau_{[\text{C II}]} \rangle \simeq 1.3$, and $\langle N(\text{C}^+) \rangle \simeq 3 \times 10^{18} \text{ cm}^{-2}$. The highest C^+ column density peaks are found near the Trapezium, the Orion Bar, the East PDR, and northeast of Orion BN/KL. In these emission peaks, the excitation temperatures and line opacities ($T_{\text{ex}} = 250-300$ K and $\tau_{[\text{C II}]} \simeq 1 - 2$) are higher than the average. The 25'' beam-averaged C^+ column density toward these peaks is $N(\text{C}^+) \simeq 10^{19} \text{ cm}^{-2}$.

The inferred excitation temperatures can be used to further constrain the origin of the $[\text{C II}]$ emission at the FUV-illuminated surface of the cloud. In particular, the mean $T_{\text{ex}} \gtrsim 100$ K values inferred from the map require the fractional population of the $^2P_{3/2}$ level, $n(^2P_{3/2})/n(^2P_{1/2} + ^2P_{3/2})$, to be >0.45 . The representative PDR model in Figure 5 shows that the conditions for producing significant $[\text{C II}]$ emission are quite restrictive. For high FUV radiation fields, the C^+ layers extend

to $A_{\text{V}} \simeq 3-4$ mag, but the gas temperature falls much faster for any reasonable density. Figure 5 shows that a fractional population >0.45 of the $^2P_{3/2}$ level requires high gas densities ($n_{\text{H}} \simeq 5 \times 10^3$ for even $T_{\text{k}} \simeq 500$ K; see Figure 10). Hence, the bright $[\text{C II}]$ emission from OMC 1 traces narrow cloud surface layers ($A_{\text{V}} < 4$ mag) and not the entire line of sight.

In the extended regions, the $[^{13}\text{C II}]$ lines are not detected and the $[\text{C II}]$ 158 μm line is weaker. This suggests that the line is optically thin or effectively thin (Goldsmith et al. 2012). The line opacity can be derived if one knows T_{ex} . Here we make the approximation $\tau_{[\text{C II}]} \simeq T_{\text{P}}([\text{C II}])/J(T_{\text{ex}})$. Figure 9(a) shows a column density map, computed under these assumptions, of the blueshifted component ($v_{\text{LSR}} \simeq -2$ to $+5 \text{ km s}^{-1}$) that includes the Dark Bay and the Northern Dark Lane emission. We adopted a constant $T_{\text{ex}} \simeq 80$ K (intermediate between T_{k} in the OMC 1/H II interfaces and that in the atomic Veil; Abel et al. 2009). The resulting $N(\text{C}^+)$ toward the Dark Bay ($\simeq 1.4 \times 10^{18} \text{ cm}^{-2}$) is equivalent to $A_{\text{V}} \simeq N(\text{C}^+)/4 \times 10^{17} \simeq 3.5$ mag (i.e., significant H_2 must be present) assuming that the bulk of the gas-phase carbon is in C^+ , with an abundance of 1.4×10^{-4} (Sofia et al. 2004). This value is consistent with the extinction peak determined toward the Dark Bay (O'Dell & Yusef-Zadeh 2000). Other sightlines with $N(\text{C}^+) < 8 \times 10^{17} \text{ cm}^{-2}$ ($A_{\text{V}} < 2$ mag) are likely associated with C^+ in nearly atomic H I gas (e.g., toward the Trapezium). The integrated C^+ column density in the map ($v_{\text{LSR}} \simeq -2$ to $+5 \text{ km s}^{-1}$ component) is compatible with the observed $[\text{C II}]$ fractional luminosity of $\sim 12\%$ (Section 3.3).

In addition, Figure 9(b) shows a $N(\text{C}^+)$ map of the OMC 1 component ($v_{\text{LSR}} \simeq 5$ to $+17 \text{ km s}^{-1}$) adopting $T_{\text{ex}} \simeq 100$ K from the map averaged spectrum. Figure 9(c) shows the resulting map of the total C^+ column density along each line of sight, $N(\text{C}^+)_{\text{Total}} = N(\text{C}^+)_{\text{OMC1}} + N(\text{C}^+)_{\text{blue}} + N(\text{C}^+)_{<-2 \text{ km s}^{-1}}$, where we have added, at each position, $N(\text{C}^+)_{<-2 \text{ km s}^{-1}} = 10^{17} \text{ cm}^{-2}$ from additional foreground emission components at $v_{\text{LSR}} < -2 \text{ km s}^{-1}$. The integrated column density in the $<-2 \text{ km s}^{-1}$ component is consistent with the $\sim 3\%$ contribution to the total $[\text{C II}]$ luminosity. This is equivalent to $A_{\text{V}}^{<-2 \text{ km s}^{-1}} \simeq 0.25$ mag (i.e., fully atomic or ionized gas). We finally note that along many sightlines, the C^+ column in the Veil is comparable to that computed in the OMC 1 surface. In these approximate maps of the C^+ components without CO counterpart, $\sim 30\%$ of the C^+ mass is in CO-dark H_2 gas.

Figure 9(d) shows the $N_{\text{H}}^{\text{Total}}$ column density map obtained from the dust emission²³. Both $N(\text{C}^+)_{\text{Total}}$ and $N_{\text{H}}^{\text{Total}}$ maps can be used to estimate the fraction (f) of the total column density traced by $[\text{C II}]$ along each line of sight. In particular, Figure 9(e) shows the distribution of the $f = [N(\text{C}^+)/N_{\text{H}}]/1.4 \times 10^{-4}$ ratio at 25'' resolution. Note that this map is similar to the $L[\text{C II}]/L_{\text{FIR}}$ map shown in Figure 8(d). The lowest values $f \ll 1$ are inferred toward the high N_{H} column density ridge (bluish regions with $f \lesssim 5\%$). These fractions are consistent with the presence of a massive molecular cloud behind the $[\text{C II}]$ -emitting surfaces. The typical fractions outside the ridge are $f \simeq 20\%-30\%$ (greenish regions). Far from the Trapezium, toward the extended cloud component, fractions higher than $f \gtrsim 50\%$ are only inferred toward the most translucent lines of sight. The $[\text{C II}]$ emission toward the dense PDRs around the Trapezium is slightly optically thick, and T_{ex} is higher than the average value assumed in the f map. The corrected fraction using the column of $N(\text{C}^+) \simeq 10^{19} \text{ cm}^{-2}$ computed from $[^{13}\text{C II}]$ is $f \simeq 40\%$.

²⁶ Toward the Orion Bar and BN/KL, the $[^{13}\text{C II}] F = 2-1$ line is blended with the redshifted $[\text{C II}]$ emission. To avoid overestimating the $[\text{C II}]$ 158 μm line opacity toward these positions, we used the $[^{13}\text{C II}] F = 1-0$ line (which is not blended with any spectral feature) and assumed $I[^{13}\text{C II}] = I_{F=1-0}/0.250$.

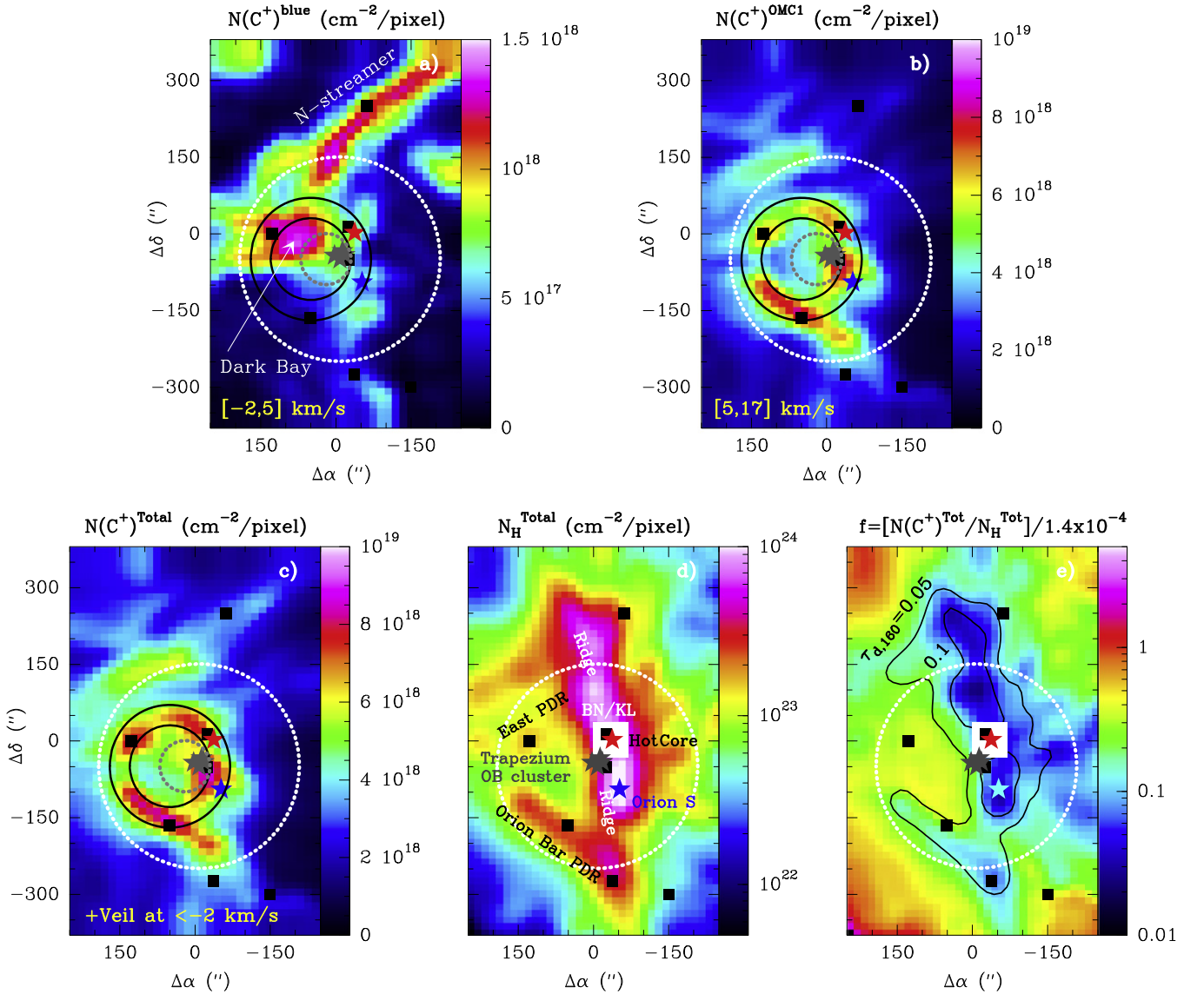


Figure 9. Column density per pixel maps toward Orion. (a) $N(\text{C}^+)_{\text{blue}}$ extracted from the blueshifted emission component from $v_{\text{LSR}} = -2$ to $+5 \text{ km}^{-1}$. (b) $N(\text{C}^+)_{\text{OMC1}}$ extracted from the main emission component from $v_{\text{LSR}} = +5$ to $+17 \text{ km}^{-1}$. (c) $N(\text{C}^+)_{\text{Total}} = N(\text{C}^+)_{\text{OMC1}} + N(\text{C}^+)_{\text{blue}} + N(\text{C}^+)_{<-2 \text{ km}^{-1}}$, where $N(\text{C}^+)_{<-2 \text{ km}^{-1}} = 10^{17} \text{ cm}^{-2}$ is adopted in all positions (see text). (d) $N_{\text{H}}^{\text{Total}} = N(\text{H}) + 2N(\text{H}_2)$ from the dust emission. (e) $f = [N(\text{C}^+)_{\text{Total}} / N_{\text{H}}^{\text{Total}}] / 1.4 \times 10^{-4}$ color map; this is roughly the fraction (f) of the total column density traced by $[\text{C II}]$ toward Orion. This fraction scales with the total column density of dust along each line of sight. The $160 \mu\text{m}$ dust opacity iso-contours at $\tau_{\text{d},160} = 0.1$ (inner) and 0.05 (outer) are shown in black. The different circles are defined in Section 3.2.

We also used the $N(\text{C}^+)$ map to compute the ‘‘PDR mass’’ in OMC 1. In particular, we integrate the equivalent $N_{\text{H,PDR}} = N(\text{C}^+)_{\text{OMC1}} / 1.4 \times 10^{-4}$ column traced by $[\text{C II}]$ as $M_{\text{PDR}} \simeq \mu m_{\text{H}} \sum_i (N_{\text{H,PDR}}^i A_i)$, where A_i is the area of pixel i , m_{H} is the H atom mass, and μ is the mean atomic weight. We derive $M_{\text{PDR}} \simeq 200 M_{\odot}$, i.e., the PDR mass fraction traced by $[\text{C II}]$ is $\sim 8\%$ (within a factor of ~ 2).

4.1.1. $[\text{C II}]$ Radiative Transfer Models

In order to constrain the range of physical conditions that reproduce the observed $[\text{C II}]$ $158 \mu\text{m}$ emission toward OMC 1, we have run a grid of nonlocal and non-LTE radiative transfer models of the ${}^2P_{3/2} - {}^2P_{1/2}$ doublet that take into account line trapping and opacity broadening (see appendix in Goicoechea et al. 2006). For consistency, we included illumination by an

FIR background continuum field and a combined treatment of gas and dust emission/absorption. Hence, at a given wavelength the opacity is given by $\tau_{\lambda} = \tau_{[\text{C II}]} + \tau_{\text{d},160}^{\text{local}}$. We used a constant column density of $N(\text{C}^+) = 3 \times 10^{18} \text{ cm}^{-2}$, the mean value we infer from the OMC 1 map, and a nonthermal velocity dispersion $\sigma_{\text{nth}} = 1.3 \text{ km s}^{-1}$ (see Section 3.3.2). The models use the most recent collisional rates of C^+ with e , H, and H_2 (with an LTE H_2 ortho-to-para ratio at each T_{k}) and assume $n_e = [\text{C}^+/\text{H}] n_{\text{H}} = 1.4 \times 10^{-4} n_{\text{H}}$ and $n(\text{H}) = 0.25 n(\text{H}_2)$ (a molecular fraction $2n(\text{H}_2)/[n(\text{H}) + 2n(\text{H}_2)]$ of $\simeq 0.9$). For gas densities $n_{\text{H}} = 2 \times 10^5 \text{ cm}^{-3}$ and $T_{\text{k}} = 500 \text{ K}$, this choice of parameters implies that the $[\text{C II}]$ ${}^2P_{3/2} - {}^2P_{1/2}$ collisional rate is due to collisions with H_2 molecules ($\sim 70\%$), H atoms ($\sim 25\%$), and electrons ($\sim 5\%$). The FIR background radiation field is modeled as thermal emission at 30 K (roughly the mean dust temperature we derive from SED fits), and the temperature of

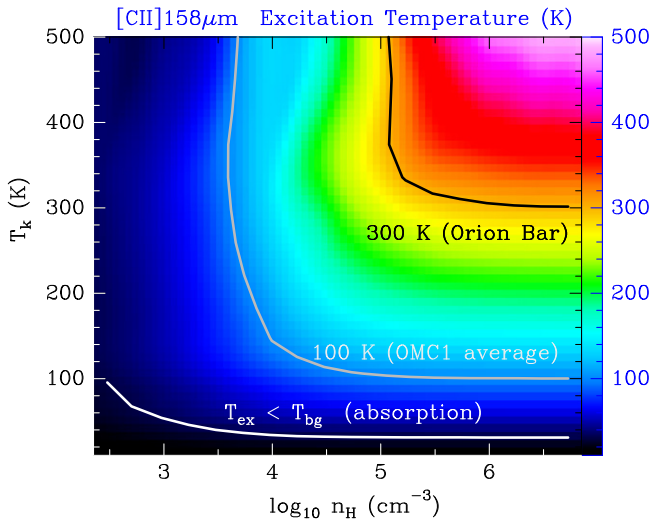


Figure 10. Synthetic excitation temperatures for the [C II] 158 μm transition obtained from a grid of nonlocal, non-LTE models (see text).

the dust grains mixed with the C^+ atoms is set to 50 K (typical of highly illuminated PDRs at $A_V \approx 2$ mag).

Figure 10 shows model results in the form of iso- T_{ex} contours. The mean [C II] excitation temperature in the *Herschel*/HIFI map is $T_{\text{ex}} \approx 100$ K. This plot shows that the minimum gas density required to produce this $T_{\text{ex}} = 100$ K is $n_{\text{H}} \approx 5 \times 10^3 \text{ cm}^{-3}$. Toward the H II /OMC 1 interfaces (the spherical shell of PDRs around the Trapezium) T_{ex} reaches higher values (~ 250 – 300 K). This sets a higher limit to the gas density of $n_{\text{H}} \geq 10^5 \text{ cm}^{-3}$ (including the Orion Bar). The more elevated temperatures in these dense PDRs ($T_{\text{k}} \geq 300$ K) are consistent with the $T_{\text{k}} = 400$ – 700 K values inferred from H_2 pure rotational lines (Allers et al. 2005) and with $T_{\text{k}} \approx 540$ K derived from H I emission, both measurements toward the Orion Bar PDR (van der Werf et al. 2013).

Finally, the presence of a foreground halo of low-excitation material can produce [C II] absorption. Such a halo will also absorb or scatter the [C II] line photons emitted inside the cloud, if the absorption is produced at similar velocities. This may be the case of components A and B of the H I absorption in the Veil. These components peak at $v_{\text{LSR}} \approx 0$ – 6 km s^{-1} (van der Werf et al. 2013) and coincide with the blue wing of the [C II] emission seen in the main spectral component. The gas temperature and density in components A and B of Orion’s Veil are estimated from H I lines to $T_{\text{k}} \approx 50$ – 80 K and $n(\text{H}) \approx 10^{2.5-3.4} \text{ cm}^{-3}$ (Troland et al. 1989; Abel et al. 2006). For the FIR background in OMC 1 and for the parameters in our grid, we do predict [C II] absorption for low-excitation gas (white line in Figure 10). Hence, the [C II] emission dips seen in some velocity intervals may be produced by [C II] absorption in the Veil (e.g., toward the Orion Bar PDR at $v_{\text{LSR}} \approx +1 \text{ km s}^{-1}$, toward the southwest ($-150''$, $-300''$) position at $v_{\text{LSR}} \approx +3 \text{ km s}^{-1}$, or toward the ($-62''$, $250''$) position in the northern streamer at $v_{\text{LSR}} \approx +6 \text{ km s}^{-1}$; see channel maps).

In any case, our [C II] excitation models confirm that the gas density in the FUV-illuminated face of OMC 1 is high. The blueshifted [C II] emission caused by the Veil also shows that the density must be relatively high in these foreground components. This agrees with the general notion that the elevated stellar density in the Orion cluster is a consequence of

hundreds of stars that formed from a remarkably dense condensation (e.g., Genzel & Stutzki 1989; Rivilla et al. 2013).

4.2. Correlation Diagrams

Figure 11 shows correlation plots between several quantities that are also used in the discussion of the unresolved [C II] extragalactic emission (one point, one galaxy). Here we present their spatial correlation in a template massive star-forming region. In these plots, the black points represent positions outside the $200''$ (0.4 pc) radius circle, the “extended cloud face” component. Green squares represent lines of sight toward the “ H II region” component around the Trapezium stars, and red triangles represent positions in the “dense PDR interface” annulus. Gray points are other positions inside the $200''$ circle that do not fall in the latter two categories.

Figure 11(a) shows that the [C II]/FIR ratio decreases with increasing FIR intensity. In OMC 1 we find that $\log([\text{C II}]/\text{FIR}) \approx -0.6 \log(I_{\text{FIR}}[\text{erg s}^{-1} \text{ cm}^{-2} \text{ sr}^{-1}]) - 2.6$, with a correlation coefficient of $\rho = -0.93$. This is reminiscent of the “[C II] deficit” observed in ULIRGs when compared to starburst and normal galaxies (e.g., Malhotra et al. 1997; Luhman et al. 1998; Graciá-Carpio et al. 2011). In a local complex like Orion, the decrease of $L[\text{C II}]/L_{\text{FIR}}$ obviously occurs at orders of magnitude lower FIR luminosities and seems dominated by the strong variations of I_{FIR} in the region. The blue line in Figure 11(a) shows a linear model for a constant [C II] intensity cloud (the median value of the map sample).

Figure 11(b) shows that I_{FIR} increases with $\tau_{\text{d},160}$. Figure 11(c) shows an $L[\text{C II}]/L_{\text{FIR}}-T_{\text{d}}$ scatter plot. In many studies in which a complete SED cannot be constructed, T_{d} is replaced by the F_{60}/F_{100} or F_{70}/F_{160} flux ratio. Theoretical models show that the photoelectric heating efficiency decreases for high G_0/n_{H} values (also producing higher dust temperatures), because grains and PAHs get more positively charged and it becomes more difficult to photo-eject additional electrons (Tielens & Hollenbach 1985a; Okada et al. 2013). As the grain charge increases for high G_0 fields, the gas heating and cooling are reduced and a larger fraction of the FUV field is converted into dust FIR luminosity (thus lower $L[\text{C II}]/L_{\text{FIR}}$ ratios can be expected). Although such a trend is suggested by Figure 11(c), the dust temperatures obtained from the SED fits, $T_{\text{d}} = 31 \pm 4 \text{ K}$ (1σ), do not change much over the mapped region, and other effects seem to dominate the observed $L[\text{C II}]/L_{\text{FIR}}$ variations at large spatial scales.

In particular, most of the dust emission in the extended cloud is consistent with a roughly constant temperature of $T_{\text{d}} \approx 30$ K. This leads to the approximately linear relation between dust opacity and FIR intensity shown in Figure 11(b). However, the inferred dust temperatures toward some lines of sight of small $\tau_{\text{d},160}$ are lower than 30 K, resulting in lower L_{FIR} values than those expected in a constant T_{d} cloud (blue line Figure 11(b)), as well as in high $L[\text{C II}]/L_{\text{FIR}}$ ratios in Figure 11(a). On the other hand, the dust is warmer toward the dense PDRs and H II region, and high I_{FIR} intensities are observed above the constant- T_{d} blue line in Figure 11(b). The higher dust temperatures toward the central of OMC 1 likely reflect higher G_0 values and also contribution from internal dust heating by embedded sources. However, their associated $L[\text{C II}]/L_{\text{FIR}}$ ratios lie above the linear model that assumes constant [C II] emission in Figure 11(a), revealing enhanced [C II] intensity toward these regions. Still, the FIR intensity increases more

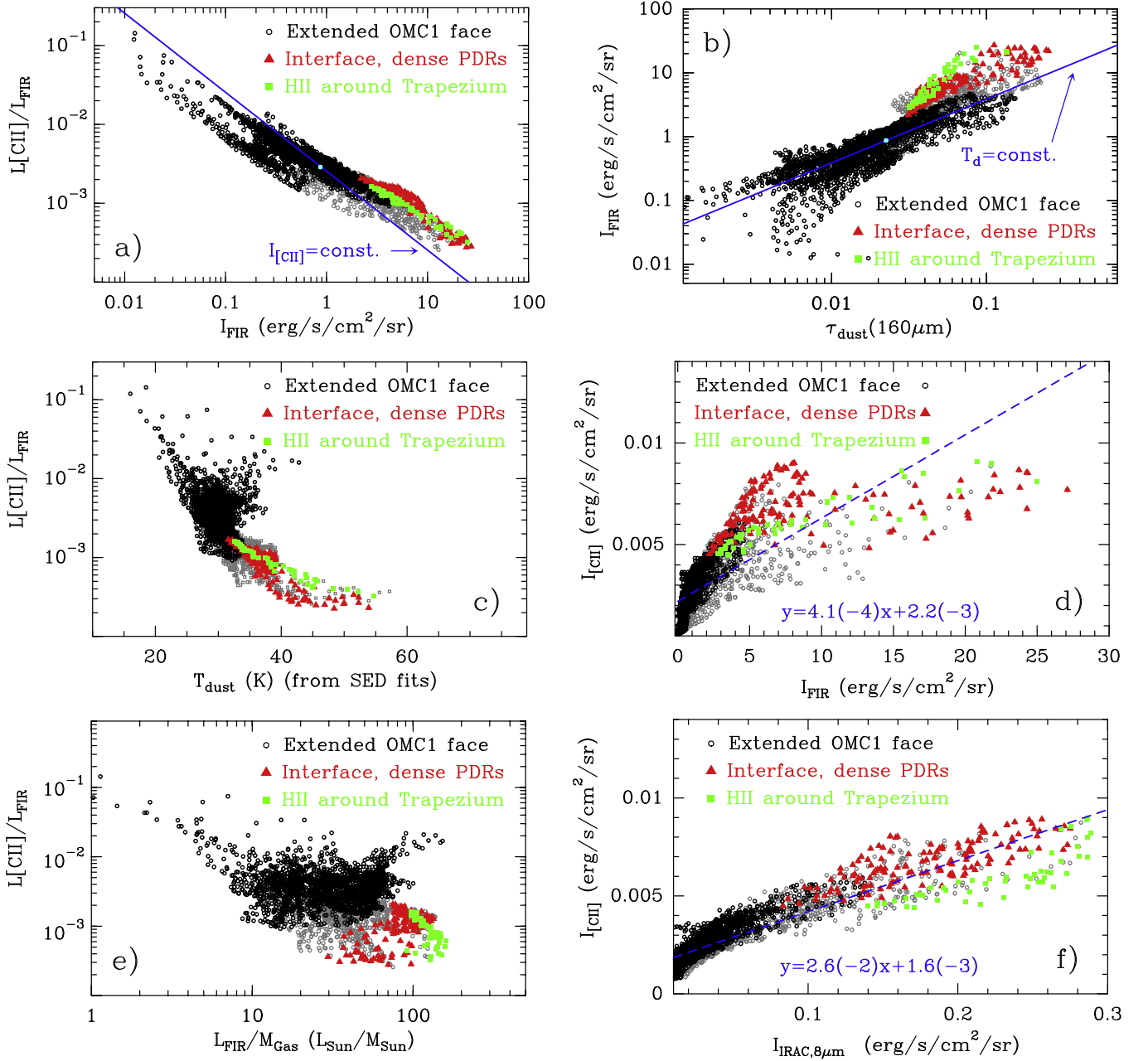


Figure 11. Correlation plots extracted from the OMC 1 maps and convolved to a uniform $25''$ resolution. Black points represent positions outside the $200''$ (0.4 pc) radius circle (“extended cloud face” component). Green squares represent positions toward the H II region component around the Trapezium. Red triangles represent positions in the “dense PDR interface” annulus (see, e.g., Figure 2). Gray points are other positions inside the $200''$ (0.4 pc) radius circle that do not fall in the latter two categories. Two models (blue lines) are plotted in panels (a) and (b), one for a constant [C II] intensity cloud (a) and another for a cloud of constant T_d (b). Both models are defined to intercept the median $L[\text{C II}]/L_{\text{FIR}}$, I_{FIR} , and $\tau_{d,160}$ of the map (cyan dots).

than [C II] (Figure 11(d)), and the resulting $L[\text{C II}]/L_{\text{FIR}}$ ratios are low toward lines of sight of high dust temperatures; see Figure 11(c) and Section 5.4.1.

Figure 11(d) shows that, except for high FIR intensities, the [C II] $158 \mu\text{m}$ intensities are reasonably well correlated with the FIR emission ($\rho = 0.75$), with $I_{[\text{C II}]} \simeq 4.1 \times 10^{-4} I_{\text{FIR}} + 2.2 \times 10^{-3}$ (in $\text{erg s}^{-1} \text{cm}^{-2} \text{sr}^{-1}$ units). The [C II] intensities, however, are better correlated with the PAH emission traced by the IRAC $8 \mu\text{m}$ image ($\rho = 0.91$, Figure 11(f)), with $I_{[\text{C II}]} \simeq 2.6 \times 10^{-2} I_{\text{IRAC } 8 \mu\text{m}} + 1.6 \times 10^{-3}$ (also in $\text{erg s}^{-1} \text{cm}^{-2} \text{sr}^{-1}$ units). As opposed to FIR, this correlation seems to hold for

high [C II] and PAH intensities. Finally, Figure 11(e) shows a correlation plot of $L[\text{C II}]/L_{\text{FIR}}$ with $L_{\text{FIR}}/M_{\text{Gas}}$. This plot shows much more scatter, but suggests that $L[\text{C II}]/L_{\text{FIR}}$ decreases from the extended cloud to the “H II region” component (highest $L_{\text{FIR}}/M_{\text{Gas}}$ values).

5. DISCUSSION

5.1. [C II], CO, and FIR Diagnostic Power

Dense PDR models predict that the low- J ^{12}CO lines saturate ($\tau \gg 1$) close to the CO abundance peak and thus the

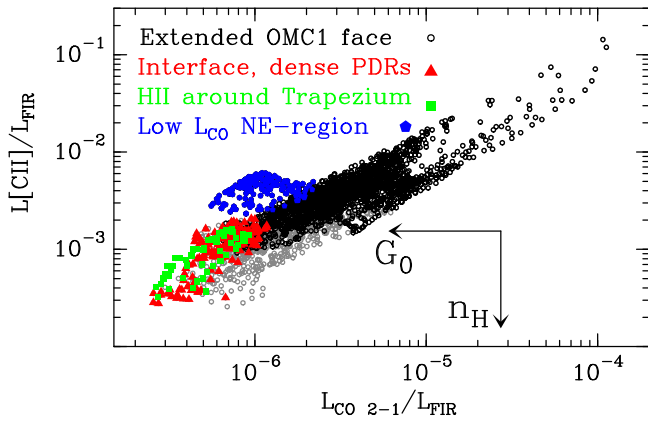


Figure 12. Same as Figure 11 but for $L[\text{C II}]/L_{\text{FIR}}$ vs. $L_{\text{CO}2-1}/L_{\text{FIR}}$. The blue pentagons represent lines of sight of low $L(\text{CO})$ and high $L[\text{C II}]/L_{\text{FIR}}$ ratios (up to ~ 5000) at the northeast of the map; see Figures 8(c) and (e). Arrows show the approximate directions of increasing G_0 and increasing n_{H} expected from PDR models (e.g., Kaufman et al. 1999; Stacey et al. 2010).

$L[\text{C II}]/L_{\text{CO}}$ ratio depends mostly on $N(\text{C}^+)$ and T_k , i.e., on G_0 and n_{H} (see, e.g., PDR models by Kaufman et al. 1999). For densities below $n_{\text{cr}} \sim 10^4 \text{ cm}^{-3}$ and $G_0 < 10^3$, the $[\text{C II}]$ 158 μm line dominates the gas cooling (Kaufman et al. 1999) and the $L[\text{C II}]/L_{\text{FIR}}$ ratio provides a good approximation to the grain photoelectric heating efficiency. For higher densities or G_0 values (i.e., the OMC 1/H II interfaces around the Trapezium), $[\text{C II}]$ collisional de-excitation plays a role and $[\text{O I}]$ starts to dominate the warm gas cooling. $[\text{O I}]$ 63 and 145 μm lines are certainly useful (Herrmann et al. 1997) although they are also bright in dissociative shocks where the $[\text{C II}]$ line is faint (e.g., Goicoechea et al. 2015). In addition, the opacity of the $[\text{O I}]$ 63 μm line is higher ($\tau_{[\text{O I}]} = 1.6\tau_{[\text{C II}]}$ for an $[\text{O}/\text{C}] = 2.2$ abundance ratio) and lies at wavelengths of higher dust opacity (2.5–6.3 times higher for $\beta = 1-2$). The $[\text{O I}]$ 63 μm line opacity problem is difficult to circumvent, because ^{18}O does not have nuclear spin (producing hyperfine splittings in $^{13}\text{C}^+$), and the isotopic shift with respect to ^{16}O is only $\sim 1.5 \text{ km s}^{-1}$ (+23.5 MHz; Brown et al. 1993). Therefore, $[\text{C II}]$ is a robust tracer of the presence of FUV photons also in dense gas.

As noted in the literature, $L[\text{C II}]/L_{\text{FIR}}$ approximately follows $L_{\text{CO}2-1}/L_{\text{FIR}}$ (Figure 12). For most of the mapped positions, the observed luminosities appear well correlated ($\rho = 0.89$ and slope of $\simeq 775$). Stacey et al. (1991a) suggested that, to a first approximation, the $L[\text{C II}]/L_{\text{FIR}}$ and $L_{\text{CO}}/L_{\text{FIR}}$ luminosity ratios can be compared with PDR models to constrain the FUV radiation field and the gas density. Most of the points in Figure 12 roughly lie on a straight line. In the frame of PDR models (e.g., Kaufman et al. 1999) this line approximately follows the decrease of G_0 (from left to right) and the decrease of n_{H} (from bottom to top). Comparing our spatially resolved luminosity ratios²⁷ (Figure 12) with the plot in Figure 5 of Stacey et al. (2010), based on PDR models of Kaufman et al. (1999) for an $A_V = 10$ mag slab, one sees that the lowest $L[\text{C II}]/L_{\text{FIR}} \simeq 3 \times 10^{-4}$ and $L_{\text{CO}2-1}/L_{\text{FIR}} \simeq 3 \times 10^{-6}$ values near the Trapezium are consistent with $G_0 \gtrsim 10^4$ and $n_{\text{H}} \gtrsim 10^5 \text{ cm}^{-3}$. On the other hand, the highest $L[\text{C II}]/L_{\text{FIR}} \gtrsim 10^{-2}$ values, corresponding to $L_{\text{CO}2-1}/L_{\text{FIR}} \lesssim 10^{-4}$ ratios in the extended cloud component, are consistent with lower FUV

fields and gas densities, $G_0 > 10^2$ and $n_{\text{H}} \approx 10^{3-4} \text{ cm}^{-3}$, respectively.

In addition, our maps reveal regions in which the luminosity ratios lie outside the parameter space allowed by $A_V = 10$ mag PDR models (blue pentagons in Figure 12). These are specific positions with very high $L[\text{C II}]/L_{\text{CO}2-1} \simeq 5000$ luminosities and low $\tau_{\text{d},160}$ opacities at the northeast of the map. Since they do not coincide with the H II region, we conclude that they must be associated with lower-density neutral gas at low A_V (thus low CO abundances for $G_0 \gg 1$ values). Indeed, a much better match with PDR models is found by considering the $A_V \simeq 3$ mag cloud models of Kaufman et al. (1999).

5.2. $[\text{C II}]$ and the Star Formation Rate in Orion

Herschel/HIFI has allowed the first velocity-resolved $[\text{C II}]$ survey of the Galactic plane, in which the contribution of the different ISM phases to the $[\text{C II}]$ emission has been constrained (e.g., Pineda et al. 2013). The combined $[\text{C II}]$ emission from all components added together correlates with the SFR in a similar manner as in nearby galaxies. Including observations of the Milky Way, the LMC, and several nearby galaxies dominated by star formation, Pineda et al. (2014) find $\log(\text{SFR} [M_{\odot} \text{ yr}^{-1}]) \simeq 0.89 \log(L[\text{C II}][\text{erg s}^{-1}]) - 36.3$. Using this correlation and the $[\text{C II}]$ luminosity toward OMC 1, we derive $\text{SFR} \simeq 3.8 \times 10^{-5} M_{\odot} \text{ yr}^{-1}$ in the mapped area. This is very similar to the rate obtained using $\text{SFR}(M_{\odot} \text{ yr}^{-1}) \simeq L_{\text{FIR}}/5.8 \times 10^9 L_{\odot}$ (e.g., Kennicutt 1998) and the observed luminosity toward OMC 1 ($L_{\text{FIR}} \simeq 2 \times 10^5 L_{\odot}$).

In addition, extinction maps of galactic star-forming regions suggest that the SFR correlates with the mass (M') of the UV-shielded ($A_V \gtrsim 7$ mag) dense gas ($n(\text{H}_2) > 10^4 \text{ cm}^{-3}$), the reservoir that ultimately forms stars (e.g., André et al. 2010; Lada et al. 2010, 2012). These studies suggest $\text{SFR}(M_{\odot} \text{ yr}^{-1}) \simeq (1.2-1.8) \times 10^{-8} M' (M_{\odot})$, and this correlation holds from star-forming regions to galaxies (Gao & Solomon 2004; Wu et al. 2005). Taking the masses inferred from our observations, we estimate $M' \simeq M_{\text{Gas,Total}} - M_{\text{PDR}} \simeq 2400 M_{\odot}$ (using the total mass deduced from the dust emission and subtracting the PDR contribution inferred from $[\text{C II}]$) and use the above relation to derive $\text{SFR} \simeq (2.9-4.3) \times 10^{-5} M_{\odot} \text{ yr}^{-1}$. Therefore, the different methods provide consistent SFR values in Orion.

Taking into account the mapped area, our derived SFR is equivalent to a very high SFR surface density of $\Sigma_{\text{SFR}} = (2.3-3.4) \times 10^{-5} M_{\odot} \text{ yr}^{-1} \text{ pc}^{-2}$. Together with the high surface density inferred from the mass estimates ($\Sigma_{\text{Gas}} \simeq 2000 M_{\odot} \text{ pc}^{-2}$), these values place the core of Orion at an extreme of a Kennicutt–Schmidt-type surface density relation ($\Sigma_{\text{SFR}} \propto \Sigma_{\text{Gas}}^{\alpha}$ with α close to 1). These and even higher surface densities are also inferred toward luminous galaxy mergers hosting intense star formation (Genzel et al. 2010).

5.3. $L[\text{C II}]/L_{\text{FIR}}$ Variations and Extragalactic Link

The reduced $L[\text{C II}]/L_{\text{FIR}}$ luminosity observed toward local ULIRGs ($L_{\text{FIR}} \gtrsim 10^{12} L_{\odot}$) has been difficult to interpret. Dust extinction, optically thick $[\text{C II}]$ emission, reduced photoelectric heating efficiency, or soft UV fields from less massive stars have been invoked (e.g., Luhman et al. 1998). In addition, extragalactic observations with *Herschel* suggest that the “line deficit” (relative to L_{FIR} or $L_{\text{FIR}}/M_{\text{Gas}}$) also applies to other FIR fine-structure lines such as $[\text{O I}]$, $[\text{N II}]$, or $[\text{O III}]$ arising from either PDRs or H II regions (Graciá-Carpio et al. 2011).

²⁷ Scaling our data by $L_{\text{FIR}} (40-500 \mu\text{m}) \simeq 1.5 L_{42-122 \mu\text{m}}$ and assuming $I_{\text{CO}2-1} \simeq 8 I_{\text{CO}1-0} (\text{erg s}^{-1} \text{ cm}^{-2} \text{ sr}^{-1})$ for optically thick thermalized CO gas.

The $L_{\text{FIR}}/M_{\text{Gas}}$ ratio, in particular, is expected to be proportional to the ionization parameter U (the number of H ionizing photons, $Q(\text{H})$, divided by the density n_{H} and by the distance to the ionizing stars). The FIR line deficit becomes more apparent in galaxies with very high $L_{\text{FIR}}/M_{\text{Gas}} \gtrsim 80 L_{\odot} M_{\odot}^{-1}$ values (Graciá-Carpio et al. 2011; González-Alfonso et al. 2015). This threshold has been suggested to separate normal galaxies from ultraluminous mergers characterized by very high SFRs (Genzel et al. 2010).

These authors suggest that the ISM conditions and the star formation efficiency in these galaxies are different from those in normal and starburst galaxies. In this context, the FIR line deficits (including $[\text{C II}]$) would be explained by the much higher ionization parameters and more extreme conditions of the H II /PDR regions they host (e.g., Graciá-Carpio et al. 2011). Photoionization models including dust grains indeed predict reduced $L[\text{C II}]/L_{\text{FIR}}$ values for high $\log U > -2$ parameters (Abel et al. 2009). One of the predicted effects is that grains absorb a higher fraction of the available UV photons relative to the gas, leaving fewer photons to ionize and heat the gas. Models of the radiative pressure on grains do show that dusty H II regions have a different ionization balance and that they compress the gas and dust into a dense ionized shell (Draine 2011). This is very suggestive of the shell-like structure revealed by the $[\text{C II}]$ and $\text{H41}\alpha$ emission around the Trapezium. On the other hand, Draine (2011) concludes that owing to the accumulation of gas and dust in a dense shell, the fraction of photons that ionize the gas actually increases (relative to a uniform H II region). In this context, the effects of increasing U may not be so severe.

Observational evidence for the presence of PAH and grains in H II regions is increasing (Ochsendorf & Tielens 2015). Their role in modulating the FUV field reaching the neutral cloud surface needs to be taken into account. The H II region around the Trapezium contains dust and is indeed characterized by a relatively high ionization parameter ($\log U \simeq -1.48$ and $Q(\text{H}) \sim 10^{49} \text{ s}^{-1}$; Baldwin et al. 1991). The presence of grains in the ionized nebula can be inferred from the depleted abundances of refractory elements like Mg, Si, and Fe from the gas phase (e.g., Simón-Díaz & Stasińska 2011).

In Orion, the sightlines with $L_{\text{FIR}}/M_{\text{Gas}} > 80 L_{\odot} M_{\odot}^{-1}$ show a very good spatial correspondence with the dense H II ionized gas traced by the $\text{H41}\alpha$ line and so they do trace regions of the high-ionization parameter (white thick contour in Figure 13). In particular, the highest $L_{\text{FIR}}/M_{\text{Gas}}$ ratios are observed close to the $\text{H41}\alpha$ emission peaks: the dense ionized gas toward the Trapezium cluster and also the ionization front that precedes the Orion Bar PDR. These regions are characterized by more extreme UV irradiation conditions ($G_0 > 10^4$).

We finally note that the luminosity of the large-scale vibrationally excited H_2 line emission toward OMC 1 is dominated by FUV-excited fluorescent emission in PDR gas (>98%; see Luhman et al. 1994), even though the collisionally excited (shocked) H_2 dominates the small-scale emission of high surface brightness (e.g., toward BN/KL and other outflows). Like the extended $[\text{C II}]$ emission we have mapped, this FUV-excited H_2 emission traces the FUV-illuminated face of Orion and may also dominate the extragalactic near-IR H_2 emission.

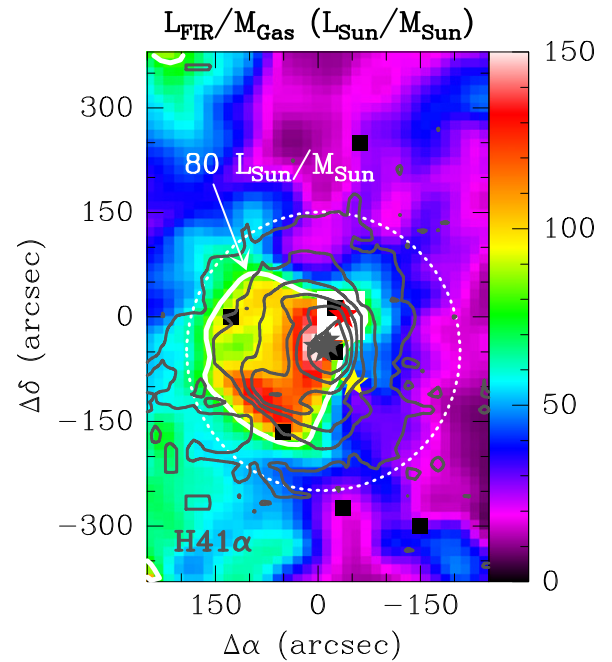


Figure 13. Spatial distribution of the $L_{\text{FIR}}/M_{\text{Gas}}$ ratio in units of $L_{\odot} M_{\odot}^{-1}$ per pixel (colored map) and $\text{H41}\alpha$ integrated intensity map in gray contours (from 2 to 22 K km s^{-1} in steps of 4 K km s^{-1}). The white thick curve shows the $L_{\text{FIR}}/M_{\text{Gas}} = 80 L_{\odot} M_{\odot}^{-1}$ iso-contour. Note the good correspondence between the ionized gas emission and the regions of high $L_{\text{FIR}}/M_{\text{Gas}}$ ratios. The red, yellow, and gray stars show the position of the Orion hot core, Orion S, and the Trapezium stars, respectively. The black squares show the positions of the spectra shown in Figure 3.

5.4. An Explanation for the “[C II] Deficit”

Figure 14 shows the spatial distribution of the two $L[\text{C II}]/L_{\text{FIR}}$ regimes found toward OMC 1. Cyan contours for low $\sim 10^{-4}$ – 10^{-3} ratios toward the core of the cloud, and red contours for high $\sim 10^{-3}$ – 10^{-2} ratios toward the extended cloud face component (increasing from the center of OMC 1 and outward). In Figure 14 (left), the $L[\text{C II}]/L_{\text{FIR}}$ contours are shown on top of the $L_{\text{FIR}}/M_{\text{Gas}}$ map. Figure 14 (right) shows the same $L[\text{C II}]/L_{\text{FIR}}$ contours on top of the $\tau_{\text{d},160}$ map.

5.4.1. Geometry and $N(\text{C}^+)$ Relative to Total N_{H} Column

Since most of the $[\text{C II}]$ emission arises from $A_V < 4$ mag FUV-irradiated cloud surface layers, the local opacity of the dust grains mixed with the C^+ atoms ($\tau_{\text{d},160}^{\text{local}}$) is generally small, $\tau_{\text{d},160}^{\text{local}} \simeq N_{\text{H}} \mu m_{\text{H}} \kappa_{160} / R_{\text{gd}} \approx 0.001$. Therefore, the dust opacity does not seem important locally, but it may be relevant if the $[\text{C II}]$ sources are embedded in large columns of dust or if many $[\text{C II}]$ -emitting surfaces in a clumpy medium are included in the telescope beam.

The average 160 μm dust opacity inside the 200'' circle region surrounding the Trapezium is only moderate ($\tau_{\text{d},160} \simeq 0.06$ or $A_V > 50$ mag). Therefore, the 160 μm continuum emission traces the column density of dust in the molecular cloud that lies behind the ionized nebula, weighted by T_{d} . The $[\text{C II}]$ emission, however, does not arise from the entire line of sight but from the FUV-illuminated face of the cloud.

Figure 15 shows the $L[\text{C II}]/L_{\text{FIR}}$ luminosity ratio as a function of $\tau_{\text{d},160}$. Both quantities are clearly tightly related.

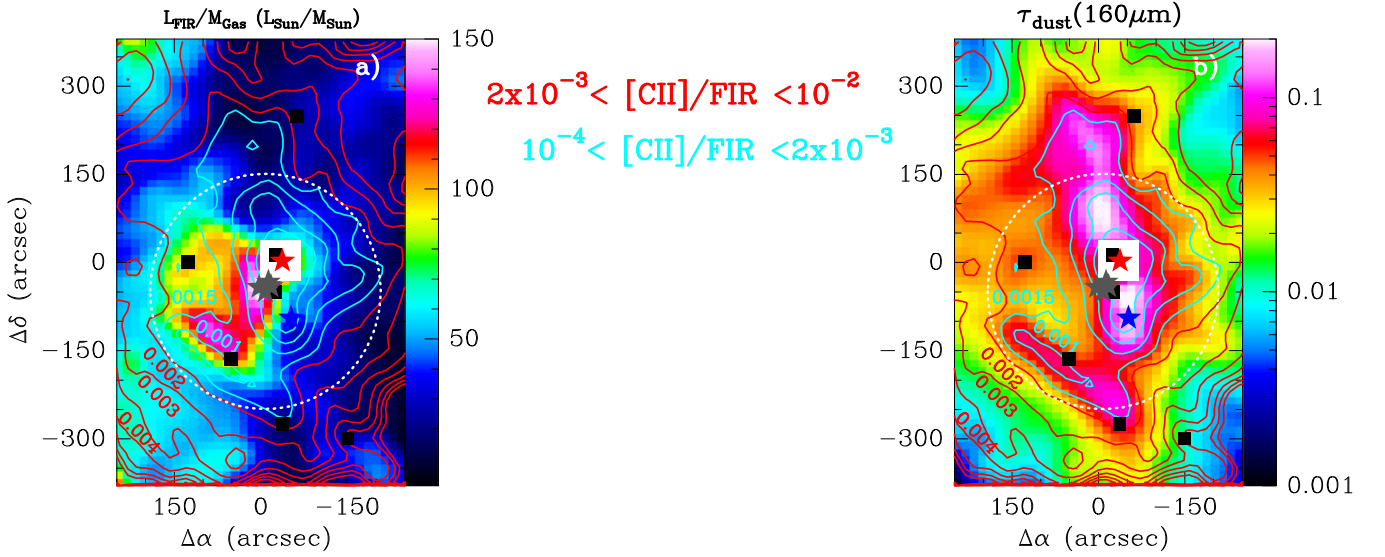


Figure 14. Spatial distribution of two regimes found for the $L[\text{C II}]/L_{\text{FIR}}$ luminosity ratio. Cyan contours for low $L[\text{C II}]/L_{\text{FIR}}$ ratios, $10^{-4} - 1.5 \cdot 10^{-3}$ toward the core of OMC 1, and red contours for high ratios, $2 \times 10^{-3} - 10^{-2}$ toward the extended cloud component (the $L[\text{C II}]/L_{\text{FIR}}$ ratio increases from the center of the map and outward). (a) The colored map shows the $L_{\text{FIR}}/M_{\text{Gas}}$ ratio, which to a first approximation traces ionized gas and the ionization parameter U . (b) The colored map shows the spatial distribution of the dust opacity at $160 \mu\text{m}$. The red, blue, and gray stars show the position of the Orion hot core, Orion S, and the Trapezium stars, respectively. The black squares denote the positions of the spectra shown in Figure 3.

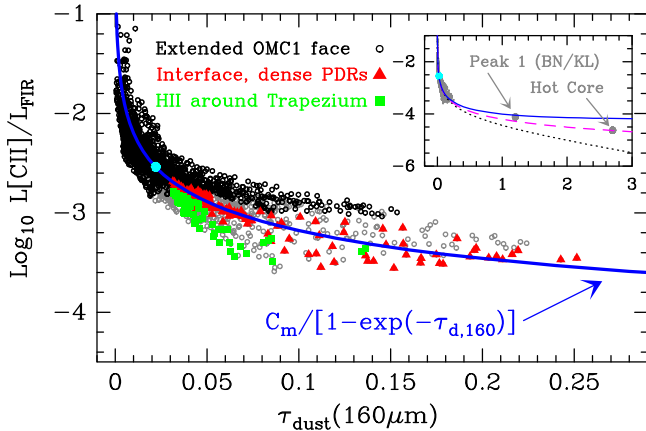


Figure 15. Observed $L[\text{C II}]/L_{\text{FIR}}$ ratios as a function of the $160 \mu\text{m}$ dust opacity. The different template regions are defined in Section 3.2. The inset panel shows an extension to higher dust opacity positions toward BN/KL. The blue solid, magenta dashed, and black dotted curves show models of constant $I[\text{C II}]/B(T_d)$ emission for different assumptions of the $[\text{C II}]$ emission location with respect to the cloud dust emission: $[\text{C II}]$ in the foreground surface (as in OMC 1), mixed C^+ gas and grains, and embedded $[\text{C II}]$ sources behind the cloud, respectively (see sketch in Figure 16). Models are defined to intercept the median $L[\text{C II}]/L_{\text{FIR}}$ and $\tau_{\text{d},160}$ values of the map (cyan dot).

Therefore, the relative geometry of the illuminating stars with respect to the molecular cloud is important to understand the variations of $L[\text{C II}]/L_{\text{FIR}}$. Toward OMC 1, it can be idealized as a slab of constant $[\text{C II}]$ emission arising from the *foreground* face of the molecular cloud (see a simplified sketch in Figure 16(a)). In this case, and for constant T_d , $L[\text{C II}]/L_{\text{FIR}}$ would vary as $1/(1 - e^{-\tau_{\text{d},160}})$, with $\tau_{\text{d},160}$ being proportional to

²⁸ In the most general case, $I[\text{C II}]/I_{\text{FIR}} \approx I[\text{C II}](T_k)/[\int B_\lambda(T_d)(1 - e^{-\tau_{\text{d},\lambda}})d\lambda]$, with T_k and T_d only coupled inside clouds at high densities $n > 10^6 \text{ cm}^{-3}$. For the 1σ range of T_d and $\tau_{\text{d},160}$ values toward OMC 1, $I[\text{C II}]/I_{\text{FIR}}$ can be approximated by $I[\text{C II}]/I_{\text{FIR}} \approx C I[\text{C II}]/[B_{160}(T_d)(1 - e^{-\tau_{\text{d},160}})]$, with the C constant varying a factor of ~ 2 depending on the exact T_d and $\tau_{\text{d},160}$ values. Thus, if T_d does not vary much, the FIR intensity raises with increasing total column density through the cloud, as shown in Figure 11(b).

the dust column toward each line of sight.²⁸ When this slab model is defined to intercept the median $L[\text{C II}]/L_{\text{FIR}}$ and $\tau_{\text{d},160}$ values of the sample, the resulting curve satisfactorily reproduces the ~ 3 orders of magnitude $L[\text{C II}]/L_{\text{FIR}}$ variations observed throughout the map (blue curve in Figure 15). The observed scatter with respect to the model is likely produced by small variations of T_d , grain charge, and of $I[\text{C II}]$ in lines of sight with the same $\tau_{\text{d},160}$ but different G_0 .

Gerin et al. (2015) have carried out small maps of the $[\text{C II}]$ $158 \mu\text{m}$ line toward a limited sample²⁹ of more distant massive star-forming regions in the Milky Way (W31C, W49N, W51, DR21(OH), ...). These observations show that the $[\text{C II}]$ absorption produced by diffuse clouds on the line of sight can reduce the $L[\text{C II}]/L_{\text{FIR}}$ ratio by $\sim 50\%$, if the v_{LSR} range of the absorbing clouds is not spectrally resolved. Velocity-*unresolved* observations toward bright FIR continuum sources with foreground diffuse clouds thus result in apparently weaker $[\text{C II}]$ luminosities. However, the most important effect revealed by the velocity-resolved $[\text{C II}]$ emission observations is the decrease of $L[\text{C II}]/L_{\text{FIR}}$ by large factors as one moves from the extended cloud component to the FIR continuum peak. Just like we have demonstrated in Orion (the $L[\text{C II}]/L_{\text{FIR}}$ and the $f = [N(\text{C}^+)/N_{\text{H}}]/1.4 \times 10^{-4}$ maps shown in Figures 8(d) and 9(e) are similar), we believe that the decrease of $L[\text{C II}]/L_{\text{FIR}}$ is due to the increase in the total column density throughout the cloud relative to the (surface) $[\text{C II}]$ emitting column.

In addition, local low-metallicity galaxies such as the nearby LMC (e.g., Leboutteiller et al. 2012), but also early galaxies at $z \sim 6$ (Capak et al. 2015), show enhanced $[\text{C II}]$ emission relative to their FIR emission. These values are interpreted as the consequence of higher penetration of FUV photons due to the lower dust content (lower extinction). This agrees with our view of galaxies having clouds of larger C^+ column densities relative to their total dust column.

²⁹ At the average distance of ~ 4 kpc of these massive star-forming regions, the $\sim 50'' \times 50''$ mapped areas are equivalent to $\sim 1 \times 1 \text{ pc}^2$. The typical spatial resolution toward these more distant SFR regions with *Herschel* is $\sim 0.2 \text{ pc}$.

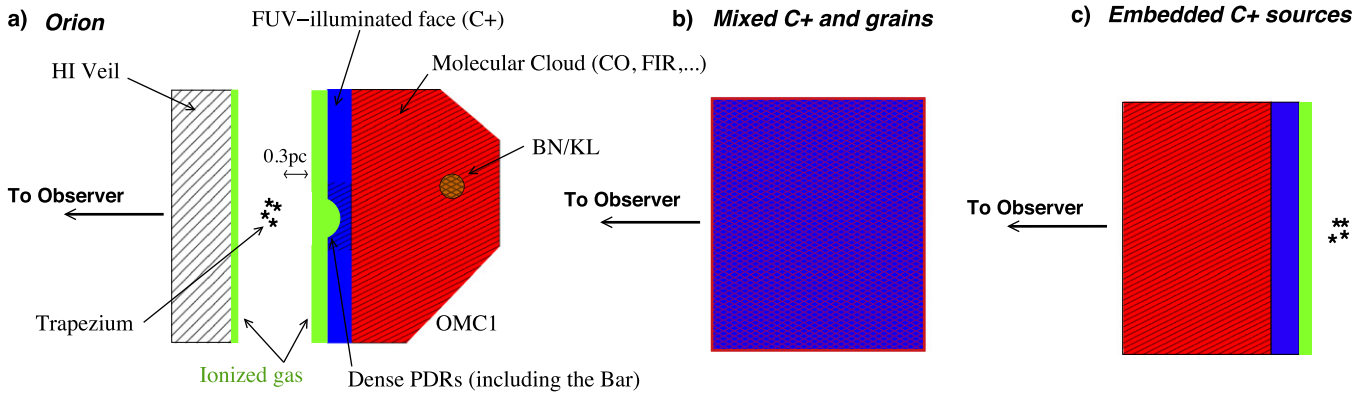


Figure 16. (a) Simplified geometry (not to scale) of OMC 1 (red, molecular gas and dust), the FUV-illuminated cloud face (blue, dominating the [C II] emission), dense ionized gas in the H II region surrounding the Trapezium (green), and the atomic Veil (shaded, producing foreground H I absorption). The observed [C II] emission, $I_{\text{[C II]}}$, reaches the observer (to the left) almost unattenuated. At a given position, the observed $\sim 160 \mu\text{m}$ dust emission is $B_{160}(T_d)(1 - e^{-\tau_{d,160}})$, where $\tau_{d,160}$ is the $\sim 160 \mu\text{m}$ dust opacity along the entire line of sight. (b) *Mixed C⁺ and dust grains* along the line of sight. In this case $I_{\text{[C II]}} = I_{0,\text{[C II]}}(1 - e^{-\tau_{d,160}})/\tau_{d,160}$, where $I_{0,\text{[C II]}}$ is the unattenuated [C II] emission. (c) [C II] sources embedded behind large columns of dust. In this case $I_{\text{[C II]}} = I_{0,\text{[C II]}}e^{-\tau_{d,160}}$.

5.4.2. Dust Attenuation

The Trapezium cluster and associated H II region are only half enveloped by the molecular cloud. The [C II]-emitting region is thus facing us and is mostly unattenuated by foreground dust. Other massive star-forming regions or galaxies may be embedded in large amounts of dust (buried starbursts in galactic nuclei in particular). In such cases, the [C II]-emission itself will be attenuated by $e^{-\tau_{d,160}}$ (a dust screen), where $\tau_{d,160}$ now represents the dust opacity between the observer and the [C II] emitting layers (Figure 16(c)). For $N(\text{H}_2) \gtrsim 10^{24} \text{ cm}^{-2}$ ($\tau_{d,160} \gtrsim 1$), the expected $L[\text{C II}]/L_{\text{FIR}}$ values can be very low, lower than 5×10^{-5} (black dotted curve in the inset of Figure 15). The prototypical example in the Milky Way is Sgr B2, the most massive starburst in the Galactic center. Sgr B2 also shows a pronounced decrease of $L[\text{C II}]/L_{\text{FIR}}$ as the dust opacity increases from the extended cloud to the (FIR) optically thick cores and embedded H II regions (e.g., Goicoechea et al. 2004; Etxaluz et al. 2013). This reasoning agrees with recent observations of local LIRGs in which the $L[\text{C II}]/L_{\text{FIR}}$ deficit is restricted to their nuclei and not their extended disks (Díaz-Santos et al. 2014).

An intermediate case may exist in which the C⁺ gas and the FIR-emitting dust grains are well mixed through the entire line of sight (Figure 16(b)). In this case, the intrinsic [C II] emission will be attenuated by $(1 - e^{-\tau_{d,160}})/\tau_{d,160}$ (e.g., Thronson et al. 1990). This model provides less extreme corrections at large extinctions (magenta dashed curve in Figure 15). Given the surface origin of the [C II] emission, this model is, however, less realistic for OMC 1, but it may apply to low metallicity galaxies (lower A_V/N_{H} and dust-to-gas mass ratios) in which larger columns of C⁺ relative to the total dust column exist owing to the much higher penetration of the FUV radiation field.

Protostellar sources in Orion BN/KL are embedded in large column densities of material, and thus very low $L[\text{C II}]/L_{\text{FIR}}$ ratios can be expected. Using the *Herschel*/PACS spectroscopic data (Goicoechea et al. 2015), we derive $L[\text{C II}]/L_{\text{FIR}} \simeq 2.4 \times 10^{-5}$ and $\tau_{d,160} \simeq 2.7$ toward the hot core and IRC sources, and $L[\text{C II}]/L_{\text{FIR}} \simeq 7.7 \times 10^{-5}$ and $\tau_{d,160} \simeq 1.2$ toward the adjacent H₂ Peak 1 outflow region. Both positions are shown in the inset panel of Figure 15. In the frame of the simple geometrical models discussed above, the $L[\text{C II}]/L_{\text{FIR}}$

ratio toward H₂ Peak 1 is still compatible with the foreground surface [C II] emission model. The $L[\text{C II}]/L_{\text{FIR}}$ ratio toward the hot core is even lower, but this is likely a consequence of the higher FIR luminosity due to internal dust heating from the protostellar sources. In any case, the embedded [C II] emission model provides extinction corrections that are too large.

5.4.3. Inhomogeneities and FUV Radiation Penetration

The structure of molecular clouds is not perfectly homogeneous (Stutzki & Guesten 1990; Falgarone et al. 1991), and FUV radiation from massive stars can penetrate to deeper cloud depths than in homogeneous clouds. Our representative (homogeneous) PDR models for $n_{\text{H}} = 2 \times 10^{5-4} \text{ cm}^{-3}$, and dust grain properties appropriate to Orion, predict $N(\text{C}^+) \simeq (1.2-1.6) \times 10^{18} \text{ cm}^{-2}$. These C⁺ column densities are a factor of $\simeq 2$ larger than the predictions of PDR models using standard ISM grain properties (Section 3.2). However, they are still lower, by a factor of ~ 3 , than the $N(\text{C}^+)$ columns inferred toward many positions of OMC 1 (see Section 4). These higher values suggest a degree of inhomogeneity at $\sim 25''$ scales ($\sim 0.05 \text{ pc}$). As noted by Stacey et al. (1993), an inhomogeneous structure facilitates the propagation of FUV photons far from the Trapezium and contributes to the increase in the fraction of the volume that is effectively producing [C II] (more surfaces along the line of sight).

6. SUMMARY AND CONCLUSIONS

We have presented the first 7.5×11.5 ($\sim 0.9 \times 1.4 \text{ pc}$) velocity-resolved map of the [C II] 158 μm line toward OMC 1. In combination with FIR photometry and H41 α and CO $J = 2-1$ line maps, we obtained the following results:

1. The main contribution to the [C II] luminosity ($\sim 85\%$) is from the extended, FUV-illuminated face of the cloud ($G_0 > 500$, $n_{\text{H}} > 5 \times 10^3 \text{ cm}^{-3}$) and from dense PDRs ($G_0 \gtrsim 10^4$, $n_{\text{H}} \gtrsim 10^5 \text{ cm}^{-3}$) at the interface between OMC 1 and the H II region surrounding the Trapezium cluster. In addition, $\sim 15\%$ of the [C II] emission arises from a different gas component without a CO counterpart. Part of this emission can be associated with filamentary structures that photoevaporate from the cloud and with depressions of the visible-light emission

previously seen in the images of the Orion Nebula (the Dark Bay, the Northern Dark Lane, and other components in the atomic H I gas Veil). An additional but minor contribution can be associated with ionized gas.

2. The highest C⁺ column density peaks are found toward the Trapezium, the Orion Bar, and specific PDRs to the east of BN/KL. These bright [C II] emission regions ($T_P \gtrsim 150$ K) follow a spherical shell structure (at least in projection on the sky) surrounding the back edge of the blister H II region. Several of these OMC 1/H II interfaces have nearly edge-on orientations. The excitation temperatures and line opacities derived from the [C II] and [¹³C II] lines are $T_{\text{ex}} = 250\text{--}300$ K and $\tau_{[\text{C II}]} \approx 1.5\text{--}3$, respectively. Hence, the [C II] line toward these peaks is slightly optically thick and traces high-excitation, dense PDR gas ($T_k \gtrsim 300$ K and $n_H \gtrsim 10^5$ cm⁻³).
3. $L[\text{C II}]/L_{\text{FIR}}$ decreases from the extended cloud component ($\sim 10^{-2}\text{--}10^{-3}$) to the cloud center ($\sim 10^{-3}\text{--}10^{-4}$). The latter are reminiscent of the “[C II] line deficit” seen toward local ULIRGs. The $L[\text{C II}]/L_{\text{FIR}}$ variations can be explained by the approximately face-on geometry of the molecular cloud relative to the externally illuminating stars. This creates a [C II] emission layer at the FUV-illuminated surface of the cloud. The FIR emission, however, approximately traces the bulk of material along each line of sight. Indeed, $L[\text{C II}]/L_{\text{FIR}}$ is spatially correlated with the dust column density in a way that agrees with a simple face-on slab model. Trying to link the local and the extragalactic emission, we conclude that the [C II]-emitting column relative to the total dust column density along each line of sight determines the observed $L[\text{C II}]/L_{\text{FIR}}$ variations, with the lowest ratios observed toward the highest column density peaks. This also implies that the specific grain properties and dust-to-gas mass ratio are important parameters in determining the $L[\text{C II}]/L_{\text{FIR}}$ luminosity ratio.
4. We show that the $L_{\text{FIR}}/M_{\text{Gas}}$ ratio follows the hydrogen-ionizing photons traced by the H41 α line, reaching $L_{\text{FIR}}/M_{\text{Gas}} > 80 L_{\odot} M_{\odot}^{-1}$ toward the H II region around the Trapezium. These high $L_{\text{FIR}}/M_{\text{Gas}}$ values are interesting proxies of the ionization parameter U and are similar to the threshold where luminous galaxies start to show “[C II] emission deficits.” Indeed, the surface densities we infer toward OMC 1 ($\Sigma_{\text{Gas}} \simeq 2000 M_{\odot} \text{pc}^{-2}$ and $\Sigma_{\text{SFR}} = (2.3\text{--}3.4) \times 10^{-5} M_{\odot} \text{yr}^{-1} \text{pc}^{-2}$) are comparable to those inferred in galaxies hosting vigorous star formation. The interesting point of course is that these conditions, those of a young massive cluster still surrounded by its dense parental molecular cloud, can dominate the FIR emission at kpc galactic scales.

The [C II] 158 μm line is undoubtedly a bright and powerful diagnostic of the FUV-illuminated ISM. In combination with other tracers ([O I], CO, dust SEDs, PAHs, and H I), a very detailed picture of the dominant environment and prevailing physical conditions can be extracted. In addition, observations of molecular ions (CO⁺, HOC⁺, CF⁺, or CH⁺) directly related to C⁺ are becoming interesting tools to constrain the properties of the “C⁺ layers” in FUV-illuminated H₂ gas (e.g., Störzer et al. 1995; Fuente et al. 2003; Neufeld et al. 2006; Guzmán et al. 2012; Nagy et al. 2013). Even more exotic ions such as OH⁺ or ArH⁺ are more specific tracers of low H₂ fraction (nearly atomic) gas, where [C II] is also expected (Neufeld et al.

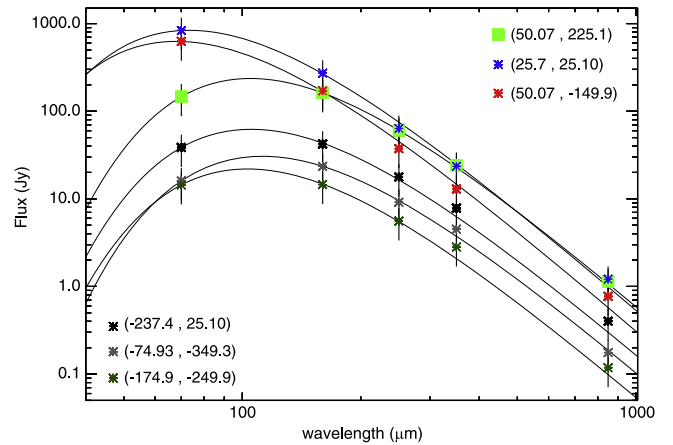


Figure 17. Example of SED fits to *Herschel*/PACS-SPIRE and *JCMT*/SCUBA2 photometric data in Jy/pixel units. All convolved at a uniform angular resolution of 25". Selected positions are indicated by their offsets with respect to the map center in arcsec.

2010; van der Tak et al. 2013; Schilke et al. 2014). Most of them can be observed with ALMA.

We acknowledge helpful comments and suggestions from our referee. We thank Spanish MINECO for funding support under grants CSD2009-00038, AYA2009-07304, and AYA2012-32032. We also thank the ERC for support under grant ERC-2013-Syg-610256-NANOCOSMOS. Part of this research was carried out at the Jet Propulsion Laboratory (JPL), California Institute of Technology (Caltech), under a contract with the National Aeronautics and Space Administration (NASA). Support for this work was provided by NASA through an award issued by JPL/Caltech. This work was supported by the German Deutsche Forschungsgemeinschaft, DFG project number SFB 956, C1. This work is in part also supported by the CNRS program “Physique et Chimie du Milieu Interstellaire (PCMI).”

Facilities: *Herschel Space Observatory*, IRAM:30m.

APPENDIX SED FITTING EXAMPLES

In this appendix we provide examples of SED fits to the FIR and submillimeter dust continuum emission (see Figure 17).

REFERENCES

- Abel, N. P. 2006, *MNRAS*, 368, 1949
 Abel, N. P., Dudley, C., Fischer, J., Satyapal, S., & van Hoof, P. A. M. 2009, *ApJ*, 701, 1147
 Abel, N. P., Ferland, G. J., O’Dell, C. R., Shaw, G., & Troland, T. H. 2006, *ApJ*, 644, 344
 Allamandola, L. J., Tielens, A. G. G. M., & Barker, J. R. 1989, *ApJS*, 71, 733
 Allers, K. N., Jaffe, D. T., Lacy, J. H., Draine, B. T., & Richter, M. J. 2005, *ApJ*, 630, 368
 André, P., Men’shchikov, A., Bontemps, S., et al. 2010, *A&A*, 518, L102
 Arab, H., Abergel, A., Habart, E., et al. 2012, *A&A*, 541, A19
 Baldwin, J. A., Ferland, G. J., Martin, P. G., et al. 1991, *ApJ*, 374, 580
 Bally, J. 2008, *Handbook of Star Forming Regions*, 1, 459
 Bally, J., Langer, W. D., Stark, A. A., & Wilson, R. W. 1987, *ApJL*, 312, L45
 Barinova, G., van Hemert, M. C., Krems, R., & Dalgarno, A. 2005, *ApJ*, 620, 537
 Berné, O., Marcelino, N., & Cernicharo, J. 2014, *ApJ*, 795, 13
 Bertoldi, F., & Draine, B. T. 1996, *ApJ*, 458, 222

- Blake, G. A., Sutton, E. C., Masson, C. R., & Phillips, T. G. 1987, *ApJ*, **315**, 621
- Boreiko, R. T., & Betz, A. L. 1996, *ApJL*, **467**, L113
- Brisbin, D., Ferkinhoff, C., Nikola, T., et al. 2015, *ApJ*, **799**, 13
- Brogan, C. L., Troland, T. H., Abel, N. P., Goss, W. M., & Crutcher, R. M. 2005, in ASP Conf. Ser. 343, *Astronomical Polarimetry: Current Status and Future Directions*, ed. A. Adamson, C. Aspin, c. J. Davis, & T. Fujiyoshi (San Francisco, CA: ASP), 183
- Brown, J. M., Evenson, K. M., & Zink, L. R. 1993, *PhRvA*, **48**, 3761
- Capak, P. L., Carilli, C., Jones, G., et al. 2015, *Natur*, **522**, 455
- Cardelli, J. A., Clayton, G. C., & Mathis, J. S. 1989, *ApJ*, **345**, 245
- Carilli, C. L., & Walter, F. 2013, *ARA&A*, **51**, 105
- Chen, J.-H., Goldsmith, P. F., Viti, S., et al. 2014, *ApJ*, **793**, 111
- Cooksey, A. L., Blake, G. A., & Saykally, R. J. 1986, *ApJL*, **305**, L89
- Crawford, M. K., Genzel, R., Townes, C. H., & Watson, D. M. 1985, *ApJ*, **291**, 755
- Cuadrado, S., Goicoechea, J. R., Pilleri, P., et al. 2015, *A&A*, **575**, A82
- Cubick, M., Stutzki, J., Ossenkopf, V., Kramer, C., & Rollig, M. 2008, *A&A*, **488**, 623
- Dalgarno, A., & McCray, R. A. 1972, *ARA&A*, **10**, 375
- de Graauw, T., Helmich, F. P., Phillips, T. G., et al. 2010, *A&A*, **518**, L6
- Díaz-Santos, T., Armus, L., Charmandaris, V., et al. 2014, *ApJL*, **788**, L17
- Draine, B. T. 2011, *ApJ*, **732**, 100
- Etzaluze, M., Goicoechea, J. R., Cernicharo, J., et al. 2013, *A&A*, **556**, A137
- Falgarone, E., Phillips, T. G., & Walker, C. K. 1991, *ApJ*, **378**, 186
- Fuente, A., Rodríguez-Franco, A., García-Burillo, S., Martín-Pintado, J., & Black, J. H. 2003, *A&A*, **406**, 899
- Gao, Y., & Solomon, P. M. 2004, *ApJ*, **606**, 271
- Genzel, R., & Stutzki, J. 1989, *ARA&A*, **27**, 41
- Genzel, R., Tacconi, L. J., Gracia-Carpio, J., et al. 2010, *MNRAS*, **407**, 2091
- Gerin, M., Ruaud, M., Goicoechea, J. R., et al. 2015, *A&A*, **573**, A30
- Goicoechea, J. R., Chavarría, L., Cernicharo, J., et al. 2015, *ApJ*, **799**, 102
- Goicoechea, J. R., & Le Boulrot, J. 2007, *A&A*, **467**, 1
- Goicoechea, J. R., Pety, J., Gerin, M., et al. 2006, *A&A*, **456**, 565
- Goicoechea, J. R., Rodríguez-Fernández, N. J., & Cernicharo, J. 2004, *ApJ*, **600**, 214
- Goldsmith, P. F., Bergin, E. A., & Lis, D. C. 1997, *ApJ*, **491**, 615
- Goldsmith, P. F., Langer, W. D., Pineda, J. L., & Velusamy, T. 2012, *ApJS*, **203**, 13
- González-Alfonso, E., Fischer, J., Sturm, E., et al. 2015, *ApJ*, **800**, 69
- Graciá-Carpio, J., Sturm, E., Hailey-Dunsheath, S., et al. 2011, *ApJL*, **728**, L7
- Graf, U. U., Simon, R., Stutzki, J., et al. 2012, *A&A*, **542**, L16
- Grenier, I. A., Casandjian, J.-M., & Terrier, R. 2005, *Sci*, **307**, 1292
- Griffin, M. J., Abergel, A., Abreu, A., et al. 2010, *A&A*, **518**, L3
- Guzmán, V., Pety, J., Gratier, P., et al. 2012, *A&A*, **543**, L1
- Habing, H. J. 1968, *BAN*, **19**, 421
- Herrera-Camus, R., Bolatto, A. D., Wolfire, M. G., et al. 2015, *ApJ*, **800**, 1
- Herrmann, F., Madden, S. C., Nikola, T., et al. 1997, *ApJ*, **481**, 343
- Hildebrand, R. H. 1983, *QJRAS*, **24**, 267
- Hogerheijde, M. R., Jansen, D. J., & van Dishoeck, E. F. 1995, *A&A*, **294**, 792
- Holland, W. S., Bintley, D., Chapin, E. L., et al. 2013, *MNRAS*, **430**, 2513
- Hollenbach, D. J., & Tielens, A. G. G. M. 1999, *RvMP*, **71**, 173
- Ingalls, J. G., Reach, W. T., & Bania, T. M. 2002, *ApJ*, **579**, 289
- Kapala, M. J., Sandstrom, K., Groves, B., et al. 2015, *ApJ*, **798**, 24
- Kaufman, M. J., Wolfire, M. G., Hollenbach, D. J., & Luhman, M. L. 1999, *ApJ*, **527**, 795
- Kennicutt, R. C., Jr. 1998, *ApJ*, **498**, 541
- Kester, D., Avruch, I., & Teyssier, D. 2014, in AIP Conf. Proc. 1636, *Bayesian Inference and Maximum Entropy Methods in Science and Engineering*, ed. R. K. Niven, B. Brewer, D. Paull, K. Shafi, & B. Stokes (New York: AIP), 62
- Lada, C. J., Forbrich, J., Lombardi, M., & Alves, J. F. 2012, *ApJ*, **745**, 190
- Lada, C. J., Lombardi, M., & Alves, J. F. 2010, *ApJ*, **724**, 687
- Langer, W. D., & Penzias, A. A. 1990, *ApJ*, **357**, 477
- Lebouteiller, V., Cormier, D., Madden, S. C., et al. 2012, *A&A*, **548**, A91
- Lee, T. A. 1968, *ApJ*, **152**, 913
- Le Petit, F., Nehmé, C., le Boulrot, J., & Roueff, E. 2006, *ApJS*, **164**, 506
- Li, A., & Draine, B. T. 2001, *ApJ*, **554**, 778
- Lilley, A. E., & Palmer, P. 1968, *ApJS*, **16**, 143
- Lis, D. C., Serabyn, E., Keene, J., et al. 1998, *ApJ*, **509**, 299
- Luhman, M. L., Jaffe, D. T., Keller, L. D., & Pak, S. 1994, *ApJL*, **436**, L185
- Luhman, M. L., Satyapal, S., Fischer, J., et al. 1998, *ApJL*, **504**, L11
- Madden, S. C., Geis, N., Genzel, R., et al. 1993, *ApJ*, **407**, 579
- Madden, S. C., Poglitsch, A., Geis, N., Stacey, G. J., & Townes, C. H. 1997, *ApJ*, **483**, 200
- Malhotra, S., Helou, G., Stacey, G., et al. 1997, *ApJL*, **491**, L27
- Malhotra, S., Kaufman, M. J., Hollenbach, D., et al. 2001, *ApJ*, **561**, 766
- Megeath, S. T., Gutermuth, R., Muzerolle, J., et al. 2012, *AJ*, **144**, 192
- Mookerjea, B., Ghosh, S. K., Kaneda, H., et al. 2003, *A&A*, **404**, 569
- Nagy, Z., Van der Tak, F. F. S., Ossenkopf, V., et al. 2013, *A&A*, **550**, A96
- Nakagawa, T., Yui, Y. Y., Doi, Y., et al. 1998, *ApJS*, **115**, 259
- Neufeld, D. A., Goicoechea, J. R., Sonnentrucker, P., et al. 2010, *A&A*, **521**, L10
- Neufeld, D. A., Schilke, P., Menten, K. M., et al. 2006, *A&A*, **454**, L37
- Ochsendorf, B. B., & Tielens, A. G. G. M. 2015, *A&A*, **576**, A2
- O'Dell, C. R. 2001, *ARA&A*, **39**, 99
- O'Dell, C. R., Henney, W. J., Abel, N. P., Ferland, G. J., & Arthur, S. J. 2009, *AJ*, **137**, 367
- O'Dell, C. R., & Yusef-Zadeh, F. 2000, *AJ*, **120**, 382
- Okada, Y., Pilleri, P., Berné, O., et al. 2013, *A&A*, **553**, A2
- Ossenkopf, V., Röllig, M., Neufeld, D. A., et al. 2013, *A&A*, **550**, A57
- Phillips, T. G., Huggins, P. J., Wannier, P. G., & Scoville, N. Z. 1979, *ApJ*, **231**, 720
- Pilbratt, G. L., Riedinger, J. R., Passvogel, T., et al. 2010, *A&A*, **518**, L1
- Pineda, J. L., Langer, W. D., & Goldsmith, P. F. 2014, *A&A*, **570**, A121
- Pineda, J. L., Langer, W. D., Velusamy, T., & Goldsmith, P. F. 2013, *A&A*, **554**, A103
- Plume, R., Kaufman, M. J., Neufeld, D. A., et al. 2004, *ApJ*, **605**, 247
- Poglitsch, A., Waelkens, C., Geis, N., et al. 2010, *A&A*, **518**, L2
- Riechers, D. A., Carilli, C. L., Capak, P. L., et al. 2014, *ApJ*, **796**, 84
- Rivilla, V. M., Martín-Pintado, J., Jiménez-Serra, I., & Rodríguez-Franco, A. 2013, *A&A*, **554**, A48
- Robberto, M., Soderblom, D. R., Bergeron, E., et al. 2013, *ApJS*, **207**, 10
- Rodríguez-Fernández, N. J., Braine, J., Brouillet, N., & Combes, F. 2006, *A&A*, **453**, 77
- Rodríguez-Franco, A., Martín-Pintado, J., & Fuente, A. 1998, *A&A*, **329**, 1097
- Roelfsema, P. R., Helmich, F. P., Teyssier, D., et al. 2012, *A&A*, **537**, A17
- Rosenthal, D., Bertoldi, F., & Drapatz, S. 2000, *A&A*, **356**, 705
- Russell, R. W., Melnick, G., Gull, G. E., & Harwit, M. 1980, *ApJL*, **240**, L99
- Sanders, D. B., & Mirabel, I. F. 1996, *ARA&A*, **34**, 749
- Schilke, P., Neufeld, D. A., Müller, H. S. P., et al. 2014, *A&A*, **566**, A29
- Simón-Díaz, S., Herrero, A., Esteban, C., & Najarro, F. 2006, *A&A*, **448**, 351
- Simón-Díaz, S., & Stasińska, G. 2011, *A&A*, **526**, A48
- Sofia, U. J., Lauroesch, J. T., Meyer, D. M., & Cartledge, S. I. B. 2004, *ApJ*, **605**, 272
- Stacey, G. J., Geis, N., Genzel, R., et al. 1991a, *ApJ*, **373**, 423
- Stacey, G. J., Hailey-Dunsheath, S., Ferkinhoff, C., et al. 2010, *ApJ*, **724**, 957
- Stacey, G. J., Jaffe, D. T., Geis, N., et al. 1993, *ApJ*, **404**, 219
- Stacey, G. J., Townes, C. H., Geis, N., et al. 1991b, *ApJL*, **382**, L37
- Störzer, H., & Hollenbach, D. 1998, *ApJ*, **495**, 853
- Störzer, H., Stutzki, J., & Sternberg, A. 1995, *A&A*, **296**, L9
- Stutzki, J., & Guesten, R. 1990, *ApJ*, **356**, 513
- Tercero, B., Cernicharo, J., Pardo, J. R., & Goicoechea, J. R. 2010, *A&A*, **517**, A96
- Thronson, H. A., Jr., Majewski, S., Descartes, L., & Hereld, M. 1990, *ApJ*, **364**, 456
- Tielens, A. G. G. M., & Hollenbach, D. 1985a, *ApJ*, **291**, 722
- Tielens, A. G. G. M., & Hollenbach, D. 1985b, *ApJ*, **291**, 747
- Troland, T. H., Heiles, C., & Goss, W. M. 1989, *ApJ*, **337**, 342
- van der Tak, F. F. S., Nagy, Z., Ossenkopf, V., et al. 2013, *A&A*, **560**, A95
- van der Werf, P. P., Goss, W. M., & O'Dell, C. R. 2013, *ApJ*, **762**, 101
- Wiesenfeld, L., & Goldsmith, P. F. 2014, *ApJ*, **780**, 183
- Wilson, N. J., & Bell, K. L. 2002, *MNRAS*, **337**, 1027
- Wolfire, M. G., Hollenbach, D., & McKee, C. F. 2010, *ApJ*, **716**, 1191
- Wu, J., Evans, N. J., II, Gao, Y., et al. 2005, *ApJL*, **635**, L173
- Wyrowski, F., Schilke, P., Hofner, P., & Walmsley, C. M. 1997, *ApJL*, **487**, L11
- Zuckerman, B. 1973, *ApJ*, **183**, 863